Chemical Engineering Journal 546 (2026) 180386

Contents lists available at ScienceDirect

Chemical Engineering Journal

journal homepage: www.elsevier.com/locate/cej

Honeycomb-reinforced gradient carbon nanotube/aramid nanofiber aerogel metamaterial with excellent electromagnetic wave absorption and load-bearing performance

Anping Wang [a], Zhichun Zhang [a,*], Zibo Li [a], Yanju Liu [b,*], Jinsong Leng [a]

[a] Centre for Composite Materials and Structures, Harbin Institute of Technology (HIT), Harbin, 150080, People's Republic of China
[b] Department of Astronautic Science and Mechanics, Harbin Institute of Technology (HIT), Harbin, 150001, People's Republic of China

ARTICLE INFO

Keywords:
Aramid nanofiber
Carbon nanotube
Waxberry-like pore structure
Aerogel/honeycomb metamaterial
Electromagnetic wave absorption

ABSTRACT

Porous aerogels have emerged as promising candidates for lightweight electromagnetic wave absorption (EMWA) materials, yet their practical performance and engineering deployment are severely constrained by three long-standing bottlenecks: the inherent trade-off between interfacial impedance matching and internal electromagnetic dissipation, the strong angular dependence of EMWA performance, and the insufficient mechanical load-bearing capability. Herein, we developed a novel dot-matrix cold-source ice-templating technique in conjunction with honeycomb skeleton reinforcement to fabricate waxberry-like gradient porous aerogel/honeycomb metamaterials (WGPA/H). The influences of critical structural parameters, including aerogel pore structure and honeycomb cell size, were systematically investigated. The optimal WGPA/H delivers an exceptional minimum reflection loss (RL_{min}) of −78.5 dB and an ultrabroad effective absorption bandwidth (EAB) of 12.4 GHz. More notably, WGPA/H retains a stable ultrabroad EAB at oblique incidence angles from 5° to 60°, demonstrating excellent angle-insensitive EMWA behavior. This outstanding comprehensive EMWA performance is attributed to the synergistic coupling effect between the unique waxberry-like gradient porous structure and the periodic honeycomb array. Furthermore, WGPA/H integrates high thermostability and a compressive strength up to 4.1 MPa, fully satisfying the service requirements of complex high-temperature and high-loading scenarios. The resultant WGPA/H well preserves the intrinsic lightweight characteristic of aerogels, breaks the trade-off between impedance matching and electromagnetic loss, realizes wide-angle EMWA stability, and simultaneously achieves significantly enhanced mechanical load-bearing performance. This work provides a new structural design strategy for multifunctional EMWA devices, facilitating their practical engineering applications.

1. Introduction

In modern military operations, stealth aircraft are required to possess superior long-range combat capability [1]. To reduce fuel consumption while boosting flight speed and cruise range, it is imperative to minimize the weight of the electromagnetic wave absorption (EMWA) protective layer on stealth aircraft, without sacrificing the requisite EMWA performance [2]. In recent years, EMWA aerogels have garnered tremendous attention in the EMWA research community owing to their ultralow density, making them promising candidates for lightweight EMWA devices [3]. Nevertheless, the generally inferior mechanical strength of aerogels has greatly restricted their deployment in high-load-bearing scenarios [4]. To address this issue, researchers have embedded honeycomb skeletons as supporting frameworks into aerogel matrices to improve their load-bearing performance [5,6]. For instance, Su et al. developed an aerogel/honeycomb hybrid metamaterial by integrating low-dielectric honeycomb frameworks with reduced graphene oxide aerogels featuring intrinsic electromagnetic characteristics [7]. By precisely filling the aerogel into honeycomb cells, this structural design not only preserves the inherent lightweight nature of both components but also overcomes the long-standing challenge of inadequate load-bearing capacity in pristine aerogels.

The electromagnetic wave attenuation and absorption capabilities of aerogels are partially ascribed to the microwave absorbers anchored on the pore walls, and more critically, to the heterogeneous porous architecture within the aerogel matrix [8]. Specifically, as electromagnetic

* Corresponding authors.
E-mail addresses: zczhang@hit.edu.cn (Z. Zhang), yj_liu@hit.edu.cn (Y. Liu).

https://doi.org/10.1016/j.cej.2026.180386
Received 8 May 2026; Received in revised form 6 July 2026; Accepted 4 August 2026
Available online 5 August 2026

waves (EMWs) undergo multiple reflections and scattering across the heterogeneous porous structure, their propagation paths inside the aerogel are effectively prolonged, and the number of interactions between EMWs and the loaded absorbers is significantly increased, thereby drastically enhancing the absorption efficiency of the microwave absorbers [9]. In addition, previous reports have demonstrated that the internal pore structure of aerogels exerts a critical impact on their EMWA performance [10–12]. For instance, Yin et al. fabricated a balsa wood-like carbon-based aerogel with an anisotropic pore structure, which features a honeycomb-like porous skeleton along the longitudinal direction and a well-ordered lamellar structure in the transverse direction [13]. Owing to the distinct structural discrepancy in pore morphology between the two orientations, the minimum reflection loss (RL_{min}) and effective absorption bandwidth (EAB) reach −61.5 dB and 6.6 GHz along the longitudinal direction, respectively, while the corresponding values are −22.4 dB and 8.49 GHz along the transverse direction. Therefore, the rational design of aerogel pore architecture is of paramount importance for tuning and optimizing the RL_{min} and EAB of aerogel-based EMWA materials.

Currently, the development of high-performance aerogel-based EMWA materials has been severely constrained by the long-standing trade-off between interfacial impedance matching and internal electromagnetic dissipation [14]. For ideal EMWA performance, two prerequisites must be satisfied simultaneously: first, the surface impedance of the aerogel must be well matched to the free-space impedance to maximize the penetration of incident EMWs into the aerogel matrix; second, the aerogel must possess sufficient electromagnetic dissipation capacity to achieve attenuation and absorption of EMWs once they propagate inside the aerogel matrix [15]. Unfortunately, conventional homogeneous aerogels with a non-gradient impedance distribution are inherently unable to reconcile these two conflicting requirements. As reported in previous literature, aerogel-based EMWA metamaterials utilize artificially designed periodic units to acquire unique gradient electromagnetic characteristics, thereby enabling efficient absorption of incident EMWs over an ultra-broad frequency range [7,16,17]. Beyond this intrinsic performance bottleneck, practical stealth application scenarios pose an additional critical challenge: when stealth aircraft perform in-flight maneuvers, the relative incidence angle (IA) of radar-emitted probing EMWs with respect to the aircraft surface changes continuously and dynamically [18]. To guarantee consistent omnidirectional radar stealth performance, the aerogel absorber must maintain stable EMWA capability over a wide range of oblique IAs [19]. Accordingly, there is an urgent and unmet demand for aerogel-based EMWA devices that can simultaneously achieve excellent interfacial impedance matching, high-efficiency internal electromagnetic dissipation, wide-angle EMWA stability, and superior mechanical load-bearing capacity.

Ice-templating is a distinctive, well-established technique for aerogel fabrication [20]. It employs ice crystals formed during the freezing of aqueous or solvent precursors as sacrificial templates. Through precise regulation of the nucleation, growth, and spatial arrangement of ice crystals, followed by ice template removal via vacuum freeze-drying, a porous aerogel architecture that faithfully replicates the morphology of ice crystals can be constructed [21]. Currently, mainstream ice-templating strategies are generally categorized into two modes: uniform freezing and unidirectional freezing [22]. In uniform freezing, samples are placed in a standard freezing chamber to undergo isotropic cooling in all directions, producing randomly distributed ice crystals with isotropic features. For instance, Liu et al. fabricated cellulose nanofiber/carbon nanotube composite aerogels via the uniform freezing approach, where the internal pore structure of the resultant aerogels presented a random, disordered distribution [23]. In unidirectional freezing, by contrast, one side of the precursor solution is brought into direct contact with a low-temperature cold source to establish a uniaxial temperature gradient. This gradient drives the oriented growth of ice crystals along the freezing direction, thereby enabling the formation of highly aligned pore architectures inside the aerogel. As a typical example, Wu et al. prepared carbon nanotube/polyimide composite aerogels using the unidirectional freezing method, and the internal pore structure of the as-fabricated aerogels exhibited a distinct parallel alignment characteristic [24]. Nevertheless, aerogels synthesized by both the aforementioned approaches show no gradient variation in electromagnetic properties along the thickness direction. Therefore, the inherent contradiction between interfacial impedance matching and internal electromagnetic dissipation still remains intractable for aerogel-based EMWA systems.

Herein, we propose an innovative dot-matrix cold-source ice-templating strategy coupled with honeycomb skeleton reinforcement. The dot-matrix cold sources are precisely engineered to regulate the three-dimensional radial growth of ice crystals within honeycomb cells, thus endowing the aerogel confined in the honeycomb cells with a waxberry-like gradient porous microstructure and periodic array. Compared with the conventional non-gradient porous aerogel/honeycomb composites, our developed waxberry-like gradient porous aerogel/honeycomb metamaterials (WGPA/H) simultaneously realize excellent interfacial impedance matching and efficient electromagnetic dissipation via the synergistic effect of the waxberry-like gradient porous structures and the periodic honeycomb arrays. Consequently, the optimized WGPA/H exhibits an ultra-low RL_{min} of −78.5 dB and an ultra-wide EAB of 12.4 GHz. More critically, WGPA/H maintains effective EMW dissipation and absorption at oblique IAs spanning from 5° to 60°, demonstrating outstanding angle-insensitive EMWA performance. Furthermore, we systematically investigated the influence of honeycomb cell size on the EMWA performance of WGPA/H, and visualized the energy dissipation distribution of EMWs in various architectures through electromagnetic numerical simulations. Benefiting from its high porosity and intrinsic thermostability, WGPA/H possesses a low bulk density along with superior flame-retardant performance. In addition, enabled by the robust mechanical support of the honeycomb framework and dense filling of the aerogel matrix, WGPA/H achieves a compressive strength of up to 4.1 MPa, corresponding to a nearly 130-fold enhancement relative to the pristine aerogel, which readily meets the stringent requirements of high-load-bearing service scenarios. Endowed with exceptional comprehensive performance, including high-efficiency EMWA, light weight, thermostability, and superior load-bearing capacity, WGPA/H holds tremendous application potential for harsh, complex service environments.

2. Experimental section

2.1. Materials

Carboxylated multi-walled carbon nanotubes (c-MWCNTs; diameter: 10–30 nm, length: 10–30 μm, purity: 98%) were obtained from Chengdu Organic Chemicals Co., Ltd., Chinese Academy of Sciences. Chopped PPTA thread (Kevlar 49) was commercially purchased from DuPont, China. Aramid honeycombs with three different cell sizes (3.2 mm, 4.8 mm, and 9.6 mm), featuring a uniform density of 48 $kg{\cdot}m^{-3}$ and a consistent thickness of 10 mm, were commercially acquired from Nanjing Bohaosheng New Material Co., Ltd., China. All chemical reagents, including dimethyl sulfoxide (DMSO), methanol (MeOH), potassium tert-butoxide (t-BuOK), and acetic acid (HAc), were supplied by Shanghai Aladdin Scientific Chemicals Co., Ltd., China.

2.2. Preparation of c-MWCNT/ANF composite dispersion

For the fabrication of the target composite dispersion, the total solid content of c-MWCNTs and aramid nanofibers (ANFs) was fixed at 5 wt%, with the filler mass ratio of c-MWCNTs to ANFs set at 4:1. This specific filler ratio was pre-optimized in our previous work, and the detailed fabrication procedures are described as follows: Briefly, 6 g of chopped Kevlar 49 fibers, 282 g of DMSO, 6 g of MeOH, and 6 g of t-BuOK were

sequentially charged into an Erlenmeyer flask equipped with a magnetic stirring bar [25]. The flask mouth was tightly sealed with Parafilm to isolate moisture from the ambient atmosphere. Subsequently, the mixture was magnetically stirred at room temperature for 24 h to induce exfoliation and homogeneous dispersion, until complete deprotonation and dissolution of the fibers were attained, affording a transparent wine-red 2 wt% ANF dispersion (Fig. S9). 24 g of c-MWCNT powder and 276 g of DMSO were sequentially added into a beaker. The resulting c-MWCNT/DMSO suspension was homogenized at 8000 rpm for 15 min using a high-shear homogenizer, coupled with 300 W water-bath sonication, to yield a preliminarily dispersed 8 wt% c-MWCNT slurry. The as-prepared 2 wt% ANF dispersion and 8 wt% c-MWCNT slurry were mixed in an equal mass ratio. Afterwards, the obtained c-MWCNT/ANF mixture was homogenized at 8000 rpm for 10 min using the aforementioned high-shear homogenizer. In this binary system, ANFs act as polymeric surfactants to facilitate the exfoliation and uniform dispersion

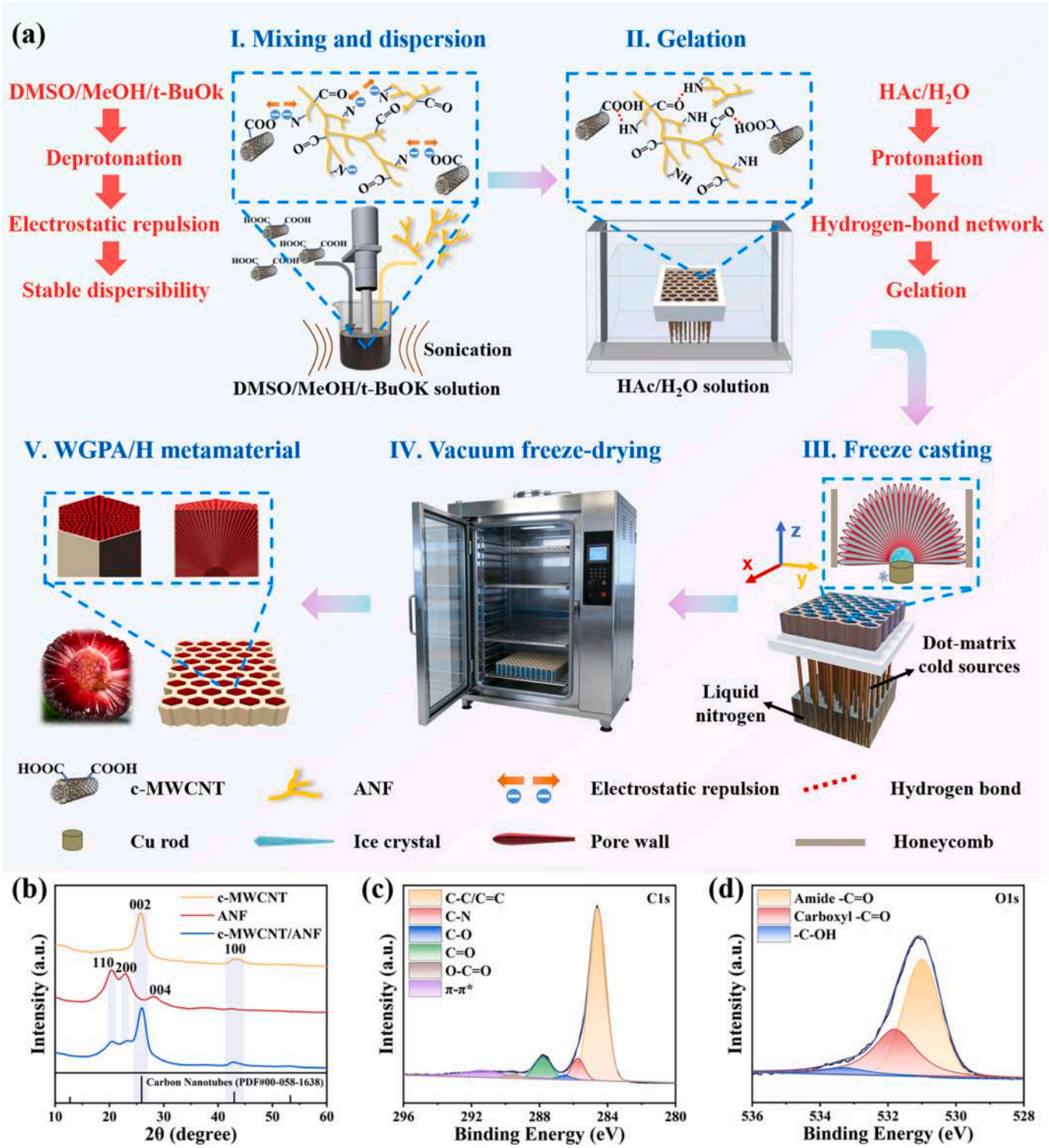

Fig. 1. (a) Schematic diagram of the preparation process and formation mechanism of WGPA/H. (b) XRD spectra. (c) XPS C1s spectra and (d) XPS O1s spectra of c-MWCNT/ANF.

of c-MWCNTs via the strong electrostatic repulsion between ANF molecular chains, thus yielding a stable c-MWCNT/ANF composite dispersion (Step I of Fig. 1 and Fig. S10).

2.3. Preparation of waxberry-like gradient porous aerogel/honeycomb metamaterials (WGPA/H)

The aramid honeycomb with a fixed cell size of 9.6 mm was employed as the structural template to fabricate a customized dot-matrix cold-source mold (Fig. S4f), where each dot cold source was precisely aligned with the center of an individual honeycomb cell. Specifically, each dot cold source was machined from a high-thermal-conductivity copper rod into a uniform cylindrical geometry, with a fixed diameter of 3 mm and a length of 60 mm. Meanwhile, the substrate and outer frame of the mold were fabricated from polytetrafluoroethylene (PTFE), featuring a standardized internal dimension of 200 × 200 × 15 mm (Fig. S1).

Taking the fabrication process of the waxberry-like gradient porous aerogel/honeycomb metamaterial with a honeycomb cell size of 9.6 mm (denoted as WGPA/H9.6) as a representative example, the detailed preparation procedure is described as follows: First, an aramid honeycomb with a thickness of 10 mm and a fixed cell size of 9.6 mm was cut into a 200 × 200 mm square plate, tailored to match the inner dimensions of the dot-matrix cold-source mold to ensure a precise and tight fit within the mold cavity. Next, the as-prepared c-MWCNT/ANF composite dispersion was slowly poured into the dot-matrix cold-source mold containing the pre-embedded aramid honeycomb, until each honeycomb cell was fully filled with the dispersion and the liquid level was exactly flush with the top surface of the honeycomb. Subsequently, the entire mold holding the dispersion-impregnated honeycomb was slowly immersed in a 1 wt% HAc aqueous solution, and kept stationary for 24 h to trigger the gelation of the composite dispersion (Step II of Fig. 1 and Fig. S11). Following complete gelation, the mold was transferred into deionized water to leach out residual HAc, and the deionized water was refreshed every 12 h until the pH of the washing solution reached neutrality. Finally, the copper pillar array at the bottom of the mold was brought into direct contact with cryogenic liquid nitrogen (Step III of Fig. 1), utilizing the dot-matrix cold sources to induce three-dimensional radial growth of ice crystals within the honeycomb-confined c-MWCNT/ANF composite hydrogel. Once the c-MWCNT/ANF hydrogel-honeycomb composite was fully frozen, the sample was carefully demolded and transferred to a freeze dryer (Step IV of Fig. 1). Freeze-drying was conducted for 72 h at a cold trap temperature of −60 °C under a vacuum pressure below 10 Pa, affording the final WGPA/H9.6 sample (Step V of Fig. 1 and Fig. S5f).

Three sets of control experiments were systematically designed based on the representative WGPA/H9.6 sample to decouple the contributions of three key structural parameters to the comprehensive performance of the composites. Initially, to elucidate the influence of the presence/absence of the honeycomb skeleton, a waxberry-like gradient porous aerogel metamaterial without a honeycomb skeleton (denoted as WGPA, Fig. S5a) was fabricated using the identical mold and preparation procedure to those employed for WGPA/H9.6. Subsequently, to clarify the effect of the aerogel internal pore structure, a random porous aerogel/honeycomb composite with a fixed honeycomb cell size of 9.6 mm was fabricated via the uniform freezing method (denoted as RPA/H9.6, Fig. S2 and Fig. S4b), and a balsa wood-like porous aerogel/honeycomb composite with a fixed honeycomb cell size of 9.6 mm was prepared using a planar cold source mold and unidirectional freezing technique (denoted as BPA/H9.6, Fig. S3 and Fig. S4c). Finally, to systematically investigate the impact of honeycomb cell size on the properties of WGPA/H series composites, waxberry-like gradient porous aerogel/honeycomb metamaterials with honeycomb cell sizes of 3.2 mm and 4.8 mm (denoted as WGPA/H3.2 and WGPA/H4.8, respectively) were prepared using the identical mold and fabrication procedure as those employed for WGPA/H9.6 (Fig. S4d and Fig. S4e). The detailed preparation process of WGPA, RPA/H9.6, BPA/H9.6, WGPA/H3.2, and WGPA/H4.8 is provided in Supporting Information.

2.4. Characterization

The morphological features of the as-prepared aerogel/honeycomb composites were characterized via three-dimensional computed tomography (3D-CT, SkyScan 1272, Bruker, USA) and scanning electron microscope (SEM, VEGA3, TESCAN, Czech Republic). The diameter of c-MWCNT was evaluated by transmission electron microscopy (TEM, JEM-F200, JEOL, Japan). For the determination of ANF diameter, atomic force microscopy (AFM, Smart SPM, AIST-NT, USA) was employed. The crystal lattice structures were examined using an X-ray diffractometer (XRD, Empyrean, PANalytical, the Netherlands). The elemental composition and chemical states of the samples were analyzed via X-ray photoelectron spectroscopy (XPS, ESCALAB 250Xi, Thermo Fisher Scientific, USA) with a monochromatic Al Kα radiation source. The thermal conductivity was measured using a hot disk thermal constant analyzer (TPS 2500S, Hot Disk AB, Sweden). Compression tests were carried out on a universal testing machine (Instron, USA) at a compression rate of 1 mm min^{-1}. The thermostability was assessed through thermogravimetric analysis (TGA 1, Mettler Toledo, Switzerland) under a nitrogen atmosphere, with a heating rate of 10 °C min^{-1} from 40 °C to 1000 °C. The relative complex permittivity and permeability in the 2–18 GHz frequency range were measured via the coaxial line method using a vector network analyzer (E5071C, Agilent, USA). For coaxial specimen preparation, molten paraffin was poured into the WGPA aerogels under vacuum-assisted conditions at 100 °C. After complete cooling and solidification, the composites were equally divided into 5 layers along the z-axis direction, and each layer was machined into coaxial rings with an outer diameter of 7 mm and an inner diameter of 3.04 mm. As illustrated in Figs. 4a and b, the reflection loss values of the samples in the 2–18 GHz frequency range were measured using the arch method with a vector network analyzer (3672C—S, Ceyear Technologies, China). During the arch method measurement, the dimensions of the test sample were 200 × 200 mm, which were identical to those of the metal backing plate. For each measurement, the reflectance of the bare metal backing plate was first tested as the reference, followed by placing the sample on the metal backing plate for measurement. The corresponding RL values were then calculated automatically by the instrument software. To investigate the angle-dependent EMWA performance, the oblique IAs of EMWs were adjusted by changing the angle between the horn antennas and the sample, which were set to 5°, 15°, 30°, 45°, and 60°, respectively. Numerical simulation of the electromagnetic power loss behavior was implemented using CST Studio Suite. (Detailed modeling and simulation parameters are provided in the Supplementary Material).

3. Results and discussion

3.1. Fabrication strategy and composition analysis

As a typical one-dimensional carbon-based material, carbon nanotubes can effectively absorb and dissipate EMWs via conductive loss mechanisms [24]. To improve their interfacial binding activity and enhance the dielectric polarization response under alternating electromagnetic fields, carboxylation-modified c-MWCNT is selected as the EMWA functional filler in this work. Nevertheless, the strong van der Waals forces and π–π stacking interactions between c-MWCNT units tend to cause severe agglomeration in solution [12]. In addition, the pristine c-MWCNT suffers from insufficient molding plasticity and mismatched electromagnetic parameters. To address these limitations, ANF is introduced as a multifunctional modifying filler, which serves multiple functions including dispersion assistance, gel solidification, and electromagnetic parameter regulation. ANF inherits the superior properties of Kevlar fibers, featuring outstanding mechanical strength, high-

temperature resistance, and flame retardancy [26]. Furthermore, upon deprotonation in strongly alkaline polar solutions, strong electrostatic repulsion arising from negative charges is generated between ANF molecular chains, endowing ANF with excellent dispersion stability [27]. More importantly, benefiting from its high aspect ratio and branched architecture, ANF enables the construction of a continuous three-dimensional network at a relatively low loading content [28].

Interaction and sol-gel transition mechanisms of the c-MWCNT/ANF system: Owing to the introduction of carboxyl functional groups on the c-MWCNT surface, the interaction forces between c-MWCNT and ANF can be tailored by adjusting the acid-base property of the solvent. As shown in Fig. S10, in strongly alkaline DMSO/MeOH/t-BuOK solution, c-MWCNT and ANF undergo deprotonation, forming ionized carboxyl groups (–COO^-) and deprotonated amine groups (–N^-). Since both the ionized –COO^- and deprotonated $-N^-$ carry negative charges, strong electrostatic repulsion exists between the c-MWCNT and ANF nanofillers in solution, thereby enabling the c-MWCNT/ANF composite solution to maintain long-term stable dispersion. Subsequently, as illustrated in Fig. S11, the DMSO/MeOH/t-BuOK solvent is replaced with an HAc/H_2O aqueous solution via a solvent exchange process. The abundant protons supplied by HAc convert –COO^- and $-N^-$ into –COOH and –NH groups, respectively. Intermolecular hydrogen bonds between –COOH and –NH groups form a three-dimensional hydrogen-bonded cross-linking network, resulting in the macroscopic sol-to-hydrogel transition of the c-MWCNT/ANF composite. Through this sol-gel transition process, the c-MWCNT functional fillers are uniformly distributed within the three-dimensional network of the hydrogel, which lays a solid foundation for the subsequent fabrication of aerogels.

The interfacial adhesion between the honeycomb skeleton and the aerogel matrix is dominated by hydrogen bonding interactions. The honeycomb skeleton is composed of poly(*m*-phenylene isophthalamide) (PMIA), whereas the ANF constituting the aerogel matrix is derived from poly(*p*-phenylene terephthalamide) (PPTA). Abundant amide groups are distributed along the molecular chains of both components. After the two components undergo sequential deprotonation in an alkaline DMSO/MeOH/t-BuOK solvent system and protonation in an acidic HAc/H_2O solvent system, interchain hydrogen bonds are formed at the interface [29], effectively improving the interfacial bonding stability of the composite system (Fig. S12).

The EMWA performance of aerogels is closely correlated with their internal pore microstructures, which serve as a core design criterion for high-performance EMWA devices. In this work, a dot-matrix cold-source mold with an embedded honeycomb was designed to induce the periodic radial growth of ice crystals within the honeycomb cells, thus forming hierarchically structured WGPA/H metamaterials (Fig. S1 and Fig. S4f). The WGPA/H, with a synergistic EMWA mechanism enabled by waxberry-like gradient pore structures and periodic arrays, resolves the trade-off between interfacial impedance matching and internal electromagnetic dissipation, exhibiting excellent EMWA performance (Fig. S20). In addition, the aerogel/honeycomb composite structure enables the lightweight design of EMWA devices, while the honeycomb embedded as a supporting skeleton significantly enhances the load-bearing capacity of the composite.

XRD was employed to analyze the crystal structures of c-MWCNT, ANF, and their corresponding composite. As presented in Fig. 1b, two diffraction peaks were detected in the XRD pattern of c-MWCNT. Specifically, the peak at $2\theta = 25.76°$ is ascribed to the typical (002) crystal plane, which reflects the ordered radial interlayer stacking of sp^2-hybridized carbon sheets in c-MWCNT; the peak at $2\theta = 42.88°$ corresponds to the (100) crystal plane, which represents the in-plane hexagonal lattice arrangement of sp^2-hybridized carbon sheets in c-MWCNT [30]. By comparing the (002) diffraction angle of the c-MWCNT ($2\theta = 25.76°$) with that of pristine carbon nanotube ($2\theta = 25.9°$), a downshift of the c-MWCNT (002) peak to a lower 2θ value was observed. This may because the carboxyl functional groups grafted on the interwall gaps and tube ends of c-MWCNT disrupt the ordered interlayer stacking and weaken the long-range crystallographic order of the carbon lamellae. Three diffraction peaks were detected at 20.40°, 22.90°, and 28.12° in the XRD pattern of ANF, corresponding to the (110), (200), and (004) crystal planes, respectively [25,31]. This result verifies the formation of a highly ordered crystalline lattice structure driven by the ordered packing of ANF molecular chains. For the c-MWCNT/ANF composite, four distinguishable diffraction peaks were observed at $2\theta = 20.51°$, 23.32°, 25.94°, and 42.70°, which are assigned to the (110), (200), (002), and (100) crystal planes, respectively [32].

High-resolution XPS C 1 s and O 1 s spectra were collected to further identify the functional group types of the c-MWCNT/ANF composite. As shown in Fig. 1c, the high-resolution C 1 s spectrum of the c-MWCNT/ANF composite could be deconvoluted into six individual component peaks, which were assigned to C–C/C=C (284.6 eV), C—N (285.8 eV), C—O (286.5 eV), C═O (287.8 eV), O–C=O (289.5 eV), and π–π* shake-up satellite (291.3 eV), respectively [33,34]. As illustrated in Fig. 1d, the high-resolution O 1 s spectrum of the c-MWCNT/ANF composite was deconvoluted into three characteristic peaks, corresponding to amide –C=O (531 eV), carboxyl –C=O (531.8 eV), and –C–OH (533.3 eV), respectively [35]. The deconvolution results of the high-resolution C 1 s and O 1 s spectra confirm that the c-MWCNT/ANF composite contains abundant polar functional groups, including carboxyl (–COOH) and amide (–CONH–) groups. Specifically, the O–C=O peak at 289.5 eV in the C 1 s spectrum, together with the carboxyl –C=O peak at 531.8 eV in the O 1 s spectrum, jointly verify the successful grafting of carboxyl groups onto the surface of c-MWCNT [36]. These polar groups are anchored at the tube ends and defect sites of c-MWCNT, forming abundant dipole active centers [26]. The presence of amide groups is corroborated by the C—N peak at 285.8 eV in the C 1 s spectrum, as well as the amide –C=O peak at 531 eV in the O 1 s spectrum [35]. Under high-frequency alternating electromagnetic fields, these polar functional groups can induce efficient dipole polarization and dissipate the energy of incident EMWs via relaxation hysteresis loss [37].

3.2. Microstructural and morphological analysis

To visualize the in situ dynamic growth behavior of ice crystals, we fabricated a transparent honeycomb mold integrated with dot-matrix cold sources. For the visualization test, deionized water was injected into the mold, and the bottom ends of copper rods were immersed in liquid nitrogen to provide a steady cryogenic cold source. The dynamic ice growth process was synchronously recorded from both side and front views using a digital camera. As illustrated in Figs. 2a and b, when the dot-matrix cold-source points were precisely positioned at the center of the honeycomb cells, the ice crystals grew radially outward from the cold-source points, forming a symmetrical radial structure (Video S1 and Video S2). In comparison, when the dot-matrix cold-source points deviated from the central axes of the honeycomb cells (Fig. S14), the growing ice crystals first contacted the adjacent honeycomb wall. Notably, it was observed that the ice crystals could propagate across the honeycomb wall via thermal conduction, while retaining their intrinsic radial growth feature (Video S3). This critical observation of cross-wall radial ice growth provides a solid experimental foundation for the scalable fabrication of WGPA/H with tunable honeycomb cell sizes using the identical dot-matrix cold-source mold.

Figs. 2c and d show photographs of the as-fabricated WGPA/H9.6 sample with dimensions of 200 × 200 mm, revealing that each honeycomb cell contains exactly one waxberry-like structural unit. We further performed 3D-CT and SEM measurements to directly visualize the hierarchical pore microstructure of the aerogel/honeycomb composite. As presented in Fig. 2e, the CT slice of WGPA/H9.6 acquired along the xy plane clearly reveals the integral honeycomb skeleton, with the aerogel matrix densely and homogeneously filled within each honeycomb cell. Fig. 2f depicts a top-view SEM micrograph of the pore structure of WGPA/H9.6, with an average pore size of approximately 400 μm. Fig. 2h displays the CT slice of the central region of a single WGPA/H9.6

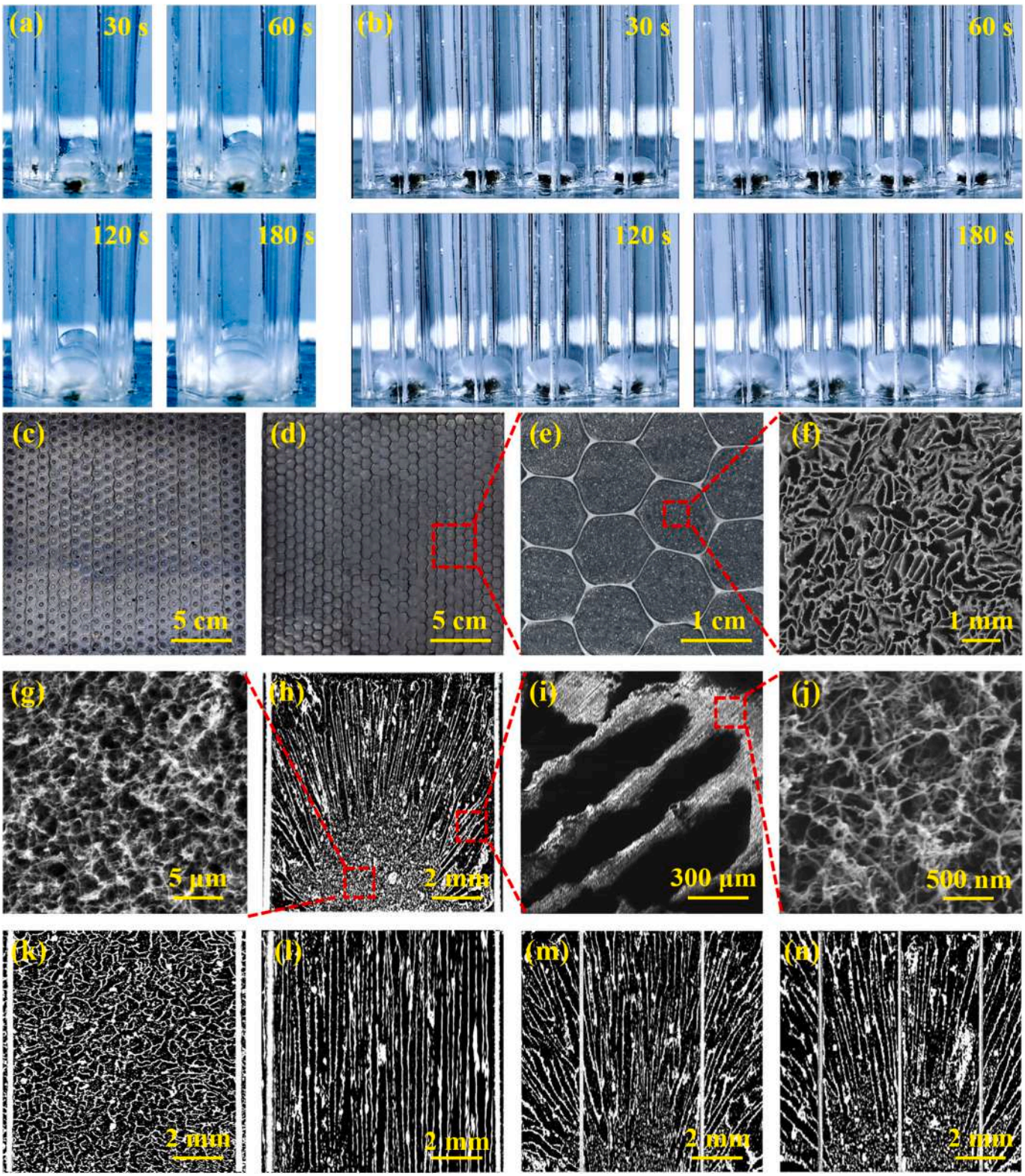

Fig. 2. Micromorphological structures. (a) Side and (b) front views of ice crystal growth process in honeycomb structures induced by dot-matrix cold sources. (c) Bottom surface of WGPA/H9.6. Top View: (d–f) Upper surface and corresponding pore structures of WGPA/H9.6. Side view: (g–j) An individual structural unit and corresponding pore structures of WGPA/H9.6. An individual structural unit of (k) RPA/H9.6, (l) BPA/H9.6, (m) WGPA/H4.8, and (n) WGPA/H3.2.

structural unit collected along the xz plane. Benefiting from ice crystal growth induced by the central cold-source point at the bottom, a hierarchical waxberry-like structure is successfully constructed inside the honeycomb cell. Specifically, the region in direct contact with the bottom cold-source point serves as the ice nucleation domain. In this region, the aerogel features pore sizes of approximately 1–2 μm without any preferential orientation, matching the core region of the waxberry structure (Fig. 2g). Radially outward from the core region, ice crystals undergo highly oriented radial growth under the induction of the intrinsic temperature gradient, endowing the resulting aerogel pores

with gradually evolved radial orientation characteristics that correspond to the pulp region of the waxberry structure. The enlarged region reveals that the terminal pore diameter of the waxberry-like pore structure is approximately 300 μm (Fig. 2i). Fig. 2j presents the high-resolution SEM image of the WGPA/H aerogel wall, where ANF and c-MWCNT construct a continuous three-dimensional network structure with abundant nanoscale micropores. Fig. S16 exhibits the nitrogen adsorption−desorption isotherms and corresponding pore size distribution of the WGPA/H aerogel. The Brunauer−Emmett−Teller (BET) specific surface area of the WGPA/H aerogel is determined to be 136.9 $m^2 g^{-1}$ (Fig. S16a). As depicted in Fig. S16b, the pore size distribution curve shows a relatively narrow distribution predominantly within the 25–60 nm range. Fig. S17 illustrates the pore morphology at the interface between two adjacent structural units of WGPA/H9.6. Since the cold-source point of WGPA/H9.6 is precisely positioned at the center of each honeycomb cell, the radial pore structure of the aerogel exhibits a symmetrical distribution relative to the honeycomb wall.

RPA/H9.6 was fabricated via uniform freezing in a freeze dryer cold trap, yielding an aerogel with a completely disordered, non-oriented pore microstructure within the honeycomb cells (Fig. 2k and Fig. S18a). In contrast, a bottom-mounted single-sided cold source was utilized for BPA/H9.6 to guide the vertically oriented growth of ice crystals, thus forming a highly aligned parallel arrangement of the aerogel pore walls inside the honeycomb cells (Fig. 2l and Fig. S18b). The three distinct pore microstructures presented in Figs. 2h, k, and l, derived from different freezing strategies, unambiguously confirm that the design and spatial layout of the cold source exert a dominant role in regulating ice crystal growth behavior, and thus fundamentally govern the final pore architecture of the resultant aerogels.

WGPA/H4.8 and WGPA/H3.2 were prepared via the same freeze-casting process as WGPA/H9.6 using the identical dot-matrix cold-source mold, and their corresponding pore microstructures are displayed in Figs. 2m and n, respectively. Notably, even though the radial growth of ice crystals within the honeycomb cells of WGPA/H4.8 and WGPA/H3.2 is physically confined by the thin honeycomb walls, the structural integrity of the waxberry-like hierarchical pore architecture is fully preserved across multiple adjacent honeycomb cells. The underlying mechanism for this phenomenon can be elaborated as follows: during the freezing process of the precursor dispersion induced by the dot-matrix cold source, when the ice crystal growth front touches the honeycomb wall interface, a temperature difference across the honeycomb wall is immediately established. Subsequently, ice nucleation is initiated on the opposite side of the honeycomb wall via thermal conduction, which effectively sustains the radial growth of ice crystals. This key mechanism is further validated by the in-situ observation of the water freezing process with dot-matrix cold-source points positioned at

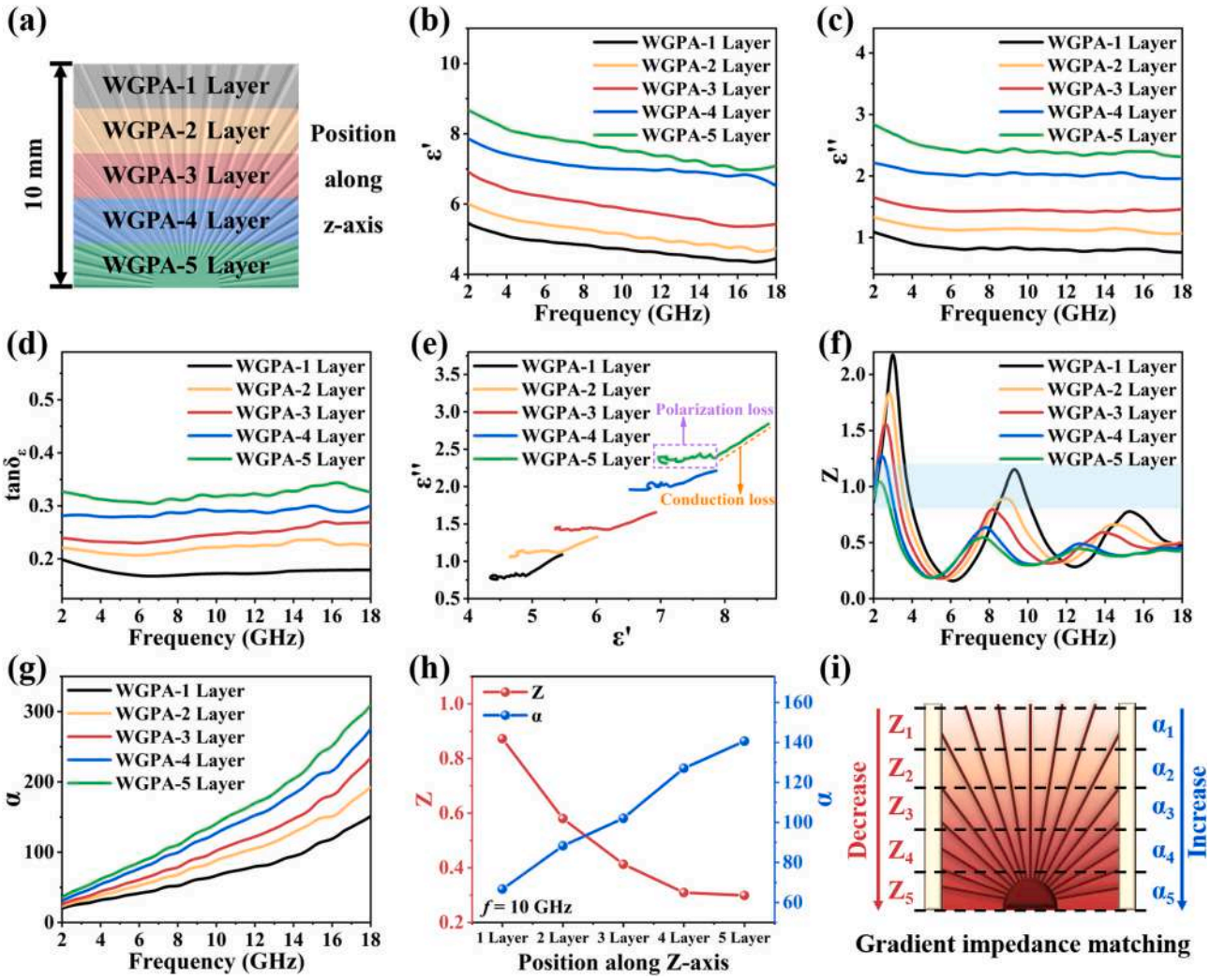

Fig. 3. Analysis of electromagnetic parameters. (a) Schematic of the layering scheme for electromagnetic parameter testing of WGPA. (b) Real part of permittivity. (c) Imaginary part of permittivity. (d) Dielectric loss tangent. (e) Cole-Cole curves. (f) Normalized characteristic impedance. (g) Attenuation constant. (h) Variation curves of normalized characteristic impedance and attenuation constant along the z-axis. (i) Schematic of the gradient impedance matching mechanism of WGPA/H.

the edge of the transparent honeycomb cells (Fig. S14), which directly confirms that the ice crystals can retain their radial growth characteristics even after crossing the honeycomb wall.

3.3. Electromagnetic parameter analysis

The electromagnetic parameters of materials are intrinsically correlated with their EMWA performance, and quantitative analysis of these parameters is critical for elucidating the underlying EMWA mechanism. In this work, the c-MWCNT/ANF composite with a c-MWCNT-to-ANF mass ratio of 4:1 was selected for systematic investigation and mechanism discussion. As shown in Fig. 3a, a 10-mm-thick WGPA aerogel was divided into five layers along the z-axis, and the electromagnetic parameters of each layer were measured. Figs. 3b and c display the real permittivity (ε') and imaginary permittivity (ε") of individual layers, which were measured over the frequency range of 2–18 GHz via the coaxial transmission line method. The results indicate that both ε' and ε" increase progressively from top to bottom along the z-axis. Such gradient variation in permittivity originates from the waxberry-like radial pore structure. The top region of the aerogel possesses a high porosity and sparse conductive network, which leads to a relatively low permittivity. Moving downward along the z-axis, the porosity of the aerogel gradually decreases and the conductive network becomes more continuous, thereby causing a continuous rise in permittivity. The dielectric loss tangent ($tan\delta_\varepsilon$) serves as a key quantitative parameter to evaluate the dielectric loss efficiency of EMWA materials, the value of $tan\delta_\varepsilon$ can be determined by the Eq. (1) [6]:

$$tan\delta_\varepsilon = \frac{\varepsilon''}{\varepsilon'} \tag{1}$$

Fig. 3d presents the $tan\delta_\varepsilon$-frequency curves of each layer, the $tan\delta_\varepsilon$ values increase gradually from top to bottom along the z-axis, demonstrating the progressive enhancement of dielectric loss capability.

Based on the Debye relaxation theory, Cole-Cole plots were constructed to investigate the polarization relaxation behavior and conduction loss mechanism, as formulated in Eqs. (2)–(4) [38,39]:

$$\varepsilon' = \varepsilon_\infty + \frac{\varepsilon_s - \varepsilon_\infty}{1 + \omega^2\tau^2} \tag{2}$$

$$\varepsilon'' = \frac{\varepsilon_s - \varepsilon_\infty}{1 + \omega^2\tau^2}\omega\tau + \frac{\sigma}{\omega\varepsilon_0} \tag{3}$$

$$\left(\varepsilon' - \frac{\varepsilon_s + \varepsilon_\infty}{2}\right)^2 + (\varepsilon'')^2 = \left(\frac{\varepsilon_s - \varepsilon_\infty}{2}\right)^2 \tag{4}$$

where ε_∞ denotes the relative permittivity at the high-frequency limit, ε_s corresponds to the static permittivity, ω represents the angular frequency, τ refers to the polarization relaxation time, and σ is the electrical conductivity. As shown in Fig. 3e, multiple semicircular arcs are clearly observed in the purple dashed-line region, indicating that the c-MWCNT/ANF composite exhibits multiple types of polarization relaxation losses during EMW attenuation. These comprehensive relaxation losses mainly originate from the dipolar polarization loss induced by the carboxyl groups and atomic vacancy defects on the c-MWCNT surface, as well as the interfacial polarization loss arising from the heterogeneous interface between c-MWCNT and ANF. Correspondingly, the orange dashed-line region denotes the presence of conductive loss for EMW attenuation in the c-MWCNT/ANF composite, which is primarily attributed to the electron migration and hopping along the interconnected c-MWCNT network.

To achieve high-efficiency EMWA, aerogels must allow incident EMWs to penetrate smoothly into the interior, which is predominantly determined by the matching degree of normalized characteristic impedance (Z) between aerogel and free space, as quantified in Eqs. (5) and (6) [40]:

$$Z_{in} = Z_0\sqrt{\frac{\mu_r}{\varepsilon_r}}\tanh\left[j\left(\frac{2\pi fd}{c}\sqrt{\mu_r\varepsilon_r}\right)\right] \tag{5}$$

$$Z = Z_{in}/Z_0 \tag{6}$$

Where Z_{in} is the input impedance of aerogel, Z_0 is the impedance of free space, f is the EMW frequency, c is the speed of light in a vacuum, and d is the thickness. ε_r ($\varepsilon_r = \varepsilon' - j\varepsilon''$) and μ_r ($\mu_r = \mu' - j\mu''$) are complex permittivity and complex permeability, respectively. The closer the value of Z is to 1, the better the impedance matching performance between the aerogel interface and free space. As can be seen from Fig. 3f, the Z values of WGPA-1 Layer range from 0.8 to 1.2 over a broad frequency band. This demonstrates that the impedance at the upper interface of WGPA is close to that of free space, allowing more EMWs to penetrate into the aerogel interior and suppressing interfacial reflection.

Once incident EMWs propagate into the interior of aerogel, the c-MWCNT/ANF composite will dissipate the EMW energy. The attenuation capability of the material can be quantified by the attenuation constant (α), as formulated in Eq. (7) [8]:

$$\alpha = \frac{\sqrt{2}}{c}\pi f \times \sqrt{(\mu''\varepsilon'' - \mu'\varepsilon') + \sqrt{(\mu''\varepsilon'' - \mu'\varepsilon')^2 + (\mu'\varepsilon'' + \mu''\varepsilon')^2}} \tag{7}$$

As shown in Fig. 3g, α exhibits a continuous upward trend with increasing frequency. This phenomenon is attributed to the enhanced polarization relaxation of the c-MWCNT/ANF composite at high frequencies, leading to more pronounced energy dissipation of the incident EMWs [9].

Fig. 3h and Fig. S19a depict the variations of Z, α, and porosity (P) against the z-axis of WGPA. It can be observed that Z and porosity present a monotonic decreasing trend, while α shows a monotonic increasing trend from top to bottom along the z-axis. Benefiting from its unique waxberry-like pore structure, WGPA exhibits gradient impedance matching characteristics along the z-axis (Fig. 3i and Fig. S19b). Such a superior structural property not only facilitates EMW penetration at the aerogel–free space interface but also promotes efficient dissipative absorption within the aerogel, thereby effectively resolving the inherent trade-off between impedance matching and electromagnetic loss.

3.4. Electromagnetic wave absorption performance

The RL_{min} and maximum effective absorption bandwidth (EAB_{max}) are widely recognized as critical metrics for evaluating the performance of EMWA devices. In this work, the EMWA performance of the as-prepared samples was directly measured via the arch method in a microwave anechoic chamber (Figs. 4a and b). The corresponding calculation formula for reflection loss (RL) is given by Eq. (8) [41]:

$$RL\ (dB) = 10log_{10}\frac{P_r}{P_0} \tag{8}$$

Where P_0 denotes the incident power, P_r represents the reflected power.

To elucidate the influence of the embedded honeycomb skeleton within the aerogel on EMW absorption performance, a comparative analysis was performed on the results presented in Figs. 4c, f, k and n. For the honeycomb-free WGPA sample, the RL_{min} reaches −40.9 dB with a corresponding EAB_{max} of 12.1 GHz. In comparison, the WGPA/H9.6 sample exhibits an ultra-low RL_{min} of −78.5 dB and an EAB_{max} of 12.4 GHz. It is evident that the introduction of the 9.6 mm-aperture honeycomb into the aerogel simultaneously increases the magnitude of RL_{min} and broadens the EAB_{max}. This performance enhancement is mainly attributed to the following mechanisms. First, the waxberry-structured aerogel is partitioned into discrete matrix-arranged structural units by the aramid honeycomb, where interunit coupling resonance effectively strengthens the EMW dissipation and absorption. In addition, the interstices between the structural units formed by the honeycomb framework provide abundant heterogeneous interfaces, which promote

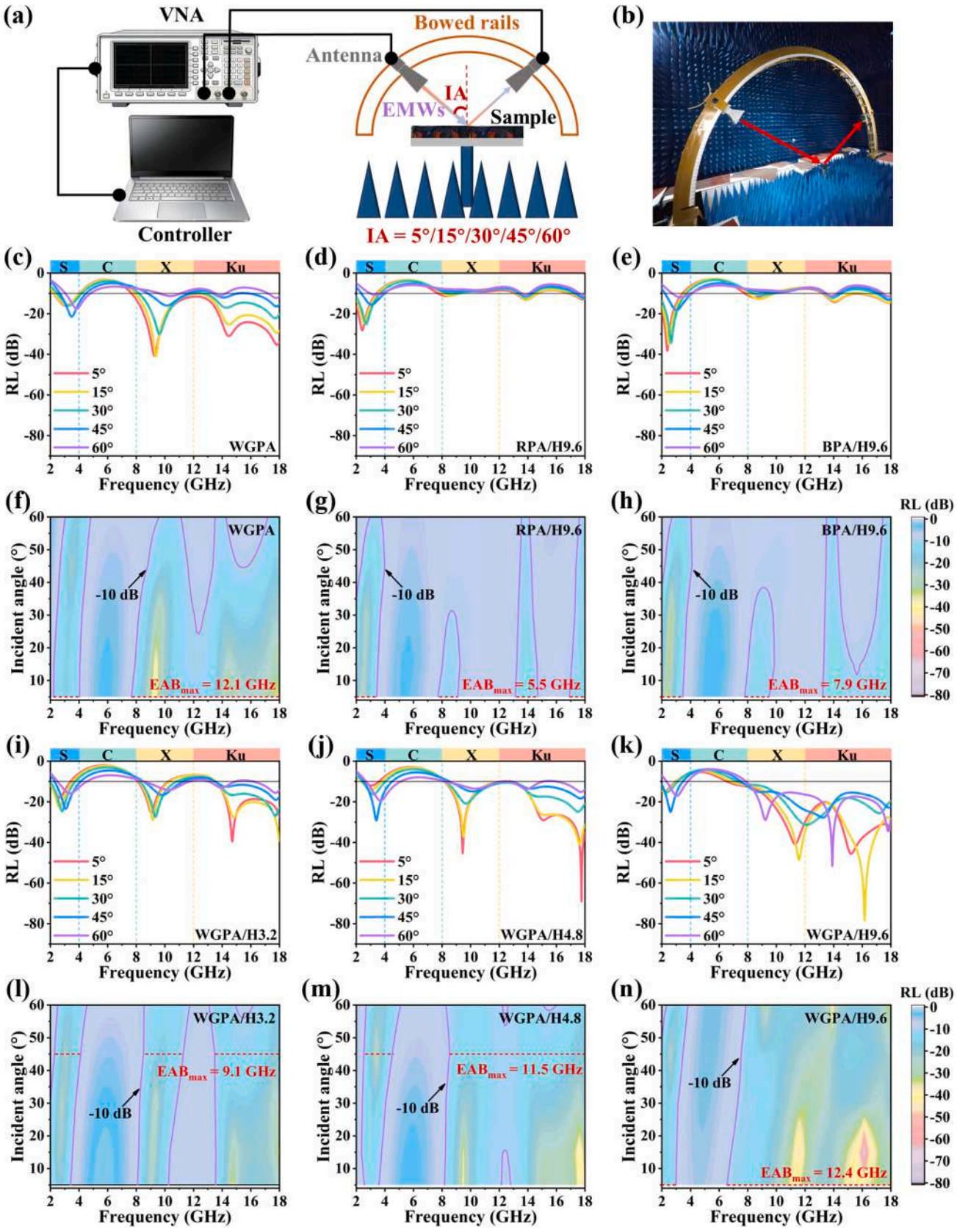

Fig. 4. (a) Schematic diagram of the arch test method and (b) photograph of the test site. (c–n) 2D RL_{min}-f-IA curves and mapping diagrams of different samples.

the multiple reflections and scattering of incident EMWs between the structural units, further boosting the EMW energy dissipation and absorption.

To ascertain the influence of the internal pore structure of the aerogel/honeycomb composites on EMWA performance under the same honeycomb cell size, a comparative analysis was conducted on the results presented in Fig. 4d, e, g, h, k and n. RPA/H9.6 exhibits an RL_{min} of −28.1 dB with a corresponding EAB_{max} of 5.5 GHz; BPA/H9.6 has an RL_{min} of −38.2 dB and an EAB_{max} of 7.9 GHz; WGPA/H9.6 delivers an ultra-low RL_{min} of −78.5 dB with an EAB_{max} of 12.4 GHz. It is evident that the EMW absorption performance of WGPA/H9.6 with a gradient pore structure is superior to that of RPA/H9.6 and BPA/H9.6 with non-gradient pore structures. The underlying enhancement mechanisms are elaborated as follows. First, along the z-axis from top to bottom, both RPA/H9.6 and BPA/H9.6 possess a uniform non-gradient pore structure, resulting in negligible variation in the EMW dissipation capacity along the wave propagation direction. In contrast, WGPA/H9.6 features a waxberry-like radial gradient pore structure with a dense central core, which constructs a gradually varying gradient impedance along the z-axis. The upper surface of WGPA/H9.6 exhibits high porosity, whose impedance matches that of free space, which endows the composite with excellent impedance-matching characteristics. This enables incident EMWs to penetrate deeper into the aerogel interior after impinging on the device surface. Second, the radial pore size of WGPA/H9.6 gradually decreases along the z-axis, which increases the number of reflections and scattering events of EMWs at the pore interfaces, thereby significantly extending the propagation path of EMWs within the aerogel. In addition, the dense central core at the bottom of WGPA/H9.6 has a low porosity, and the 3D conductive network constructed by c-MWCNTs induces intense conductive loss of EMWs via the Joule heating effect.

To investigate the influence of honeycomb cell size on EMWA performance under an identical arrangement of waxberry-structured units, a comparative analysis was performed on the results presented in Figs. 4i–n. WGPA/H3.2 exhibits an RL_{min} of −39.5 dB with a corresponding EAB_{max} of 9.1 GHz; WGPA/H4.8 achieves an RL_{min} of −69.0 dB and an EAB_{max} of 11.5 GHz; WGPA/H9.6 delivers an ultra-low RL_{min} of −78.5 dB with an EAB_{max} of 12.4 GHz. It is evident that the EMWA performance of WGPA/H improves progressively with increasing honeycomb cell size. The underlying mechanisms governing this performance trend are elaborated as follows. For WGPA/H3.2 and WGPA/H4.8, the size of a single waxberry-structured unit exceeds that of an individual honeycomb cell, thus each waxberry-structured unit is intersected by multiple honeycomb cell walls. Owing to the pronounced discrepancy in dielectric properties between the aramid honeycomb and the c-MWCNT/ANF aerogel, when incident EMWs penetrate into the aerogel interior along the radial pores of the waxberry-structured units, their propagation is inevitably impeded upon encountering these honeycomb cell walls, thereby limiting the propagation depth of EMWs along the radial pores (Fig. S21a and Fig.S21b). In contrast, the waxberry-structured units in WGPA/H9.6 are well size-matched to the honeycomb cells, where each honeycomb cell corresponds to an individual waxberry-structured unit with no extraneous honeycomb cell walls within each unit. When incident EMWs propagate into the interior of WGPA/H9.6 along its radial pores, they do not encounter any obstruction from honeycomb cell walls, enabling incident EMWs to penetrate deeper along the radial pores and thus achieving more efficient EMWA (Fig. S21c).

To validate the practical engineering reliability of WGPA/H, we further investigated the variations of its electromagnetic properties after humidity aging, thermal cycle, and compression treatments. As shown in Fig. S22, the dielectric constant of WGPA/H increased slightly after being exposed to an environment of 60 °C and 90% relative humidity for 72 h. This observation can be attributed to the polar water molecules absorbed by the porous aerogel framework, which undergo enhanced dipole polarization under high-frequency electromagnetic fields, thereby contributing to the elevated overall dielectric constant of the composite. Nevertheless, its EAB remained as high as 10.9 GHz. In addition, after three thermal cycles ranging from −40 °C to 80 °C, the dimension and EMWA performance of WGPA/H showed negligible change, which is attributed to the excellent thermal stability of the c-MWCNT and ANF functional fillers (Fig. S23). Under high-load service conditions, the aerogel, protected by the honeycomb skeleton, undergoes only small deformation and maintains reliable structural stability. However, once the applied stress exceeds the load-bearing capacity of the honeycomb skeleton, WGPA/H exhibits irreversible deformation, resulting in degraded EMWA performance (Fig. S24).

Fig. 5b and Table S3 compare the RL_{min} and EAB_{max} of WGPA/H9.6 with those of previously reported non-gradient structural aerogels [2,3,7,9,24,30,42,43]. Benefiting from the gradient engineering of the waxberry-like pore architecture and honeycomb array structure, WGPA/H9.6 delivers significantly enhanced EMWA performance relative to conventional non-gradient structural counterparts.

Additionally, the power loss density distribution of perpendicularly incident EMWs in various aerogel and aerogel/honeycomb architectures was numerically analyzed using CST Studio Suite 2025 (Fig. 5c). The detailed modeling and simulation parameters are provided in the Supporting Information. First, by comparing the power loss density distribution maps of the honeycomb-free WGPA and honeycomb-embedded WGPA/H9.6, it is found that WGPA/H9.6 exhibits a more uniform and higher-intensity power loss density distribution on its upper surface, indicating that the incorporation of the honeycomb framework significantly enhances the EMW dissipation and absorption capacity of the waxberry-structured aerogel. Subsequently, a comparative analysis of the power loss density distribution maps for aerogel/honeycomb models featuring the same honeycomb cell size but distinct aerogel pore structures (RPA/H9.6, BPA/H9.6, and WGPA/H9.6) demonstrates that incident EMWs can penetrate deep into the interior of the waxberry pore structure for efficient energy dissipation in WGPA/H9.6. This finding strongly verifies that the radial gradient pore structure of WGPA/H9.6 establishes a continuously varying gradient impedance along the thickness direction, which not only optimizes the impedance matching at the free space-aerogel/honeycomb interface but also enables highly efficient EMW dissipation and absorption within the aerogel matrix. Finally, a comparative analysis of the waxberry-structured aerogel models embedded with honeycombs of different cell sizes (WGPA/H3.2, WGPA/H4.8, and WGPA/H9.6) reveals that WGPA/H9.6, with the largest honeycomb cell size, delivers the strongest EMW dissipation intensity among the three samples. Meanwhile, incident EMWs can penetrate deep into the radial pore channels, achieving efficient EMW energy dissipation and absorption.

Fig. 5d and Video S4 demonstrate the electromagnetic wave absorption performance of the WGPA/H. As presented in the left panel of Fig. 5d, the LED bulb was successfully lit through electromagnetic induction that is driven by the high-frequency alternating electromagnetic field generated around the Tesla coil. In contrast, when WGPA/H was inserted between the Tesla coil and the LED bulb (right panel of Fig. 5d), the LED bulb was immediately extinguished. This phenomenon unequivocally verifies that WGPA/H can effectively absorb the EMWs generated by the Tesla coil.

During in-flight maneuvers of stealth aircraft, the relative angle between the aircraft and probing radar undergoes continuous dynamic changes. To guarantee omnidirectional radar stealth performance, the radar-absorbing layer is required to maintain robust and stable EMWA capability under a wide range of oblique IAs. In this study, we demonstrate that embedding honeycomb arrays into aerogel matrices can effectively mitigate their angular sensitivity under wide-angle oblique incidence of EMWs. As shown in Fig. S27a, the pristine WGPA, RPA, and BPA samples (without honeycomb embedding) exhibit a continuous reduction in EAB as the oblique IA of EMWs increases, featuring a pronounced angular dependence. In stark contrast, the WGPA/H9.6 sample with an embedded honeycomb array maintains an almost unchanged EAB across the entire oblique incidence range of 5° to 60°, exhibiting

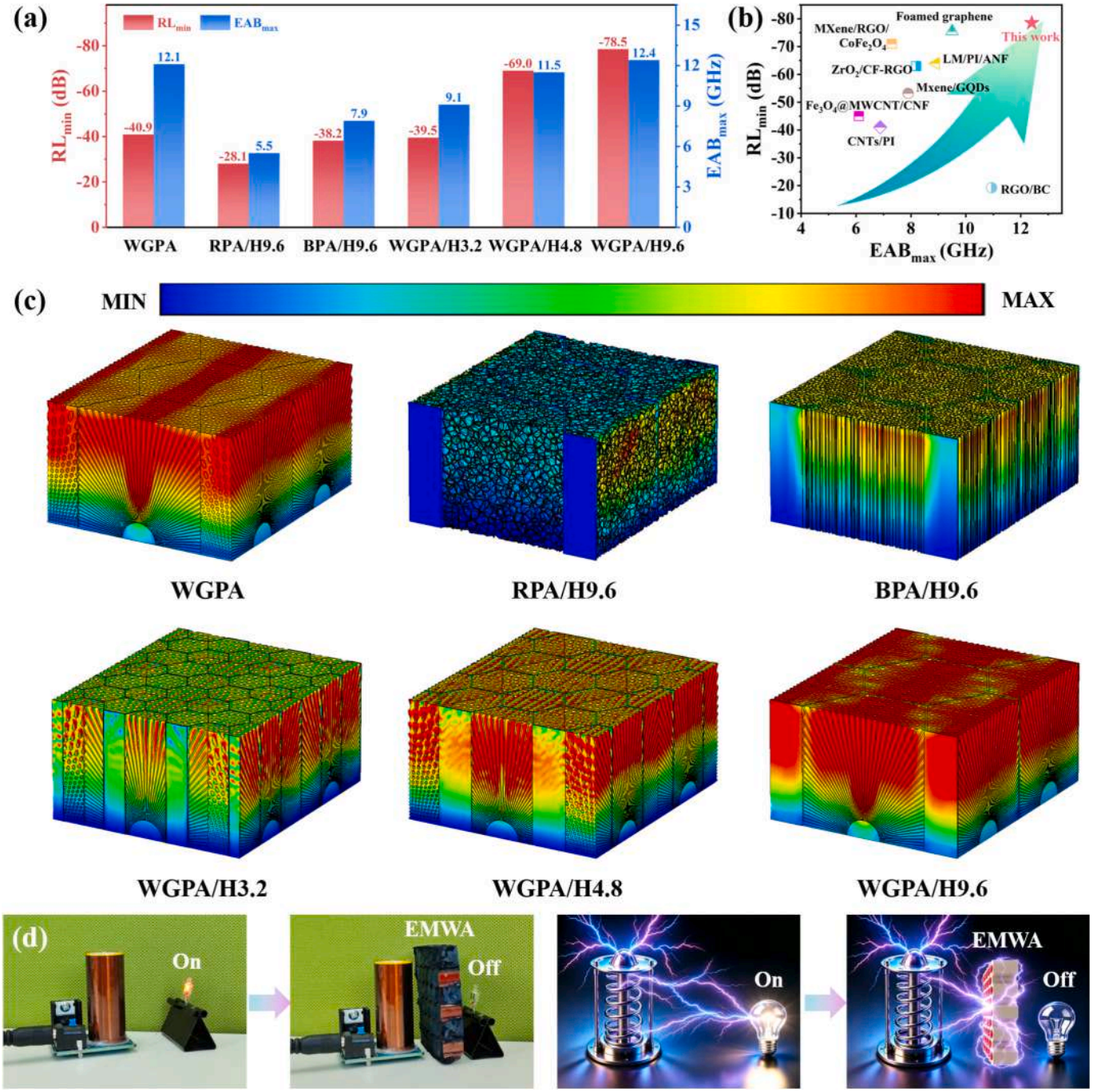

Fig. 5. (a) RL_{min} and EAB_{max} for different samples. (b) Comparison of EMWA properties between WGPA/H9.6 and traditional non-gradient structural aerogels. (c) Power loss density distribution maps of various aerogel and aerogel/honeycomb architectures. (d) Demonstration of electromagnetic wave absorption performance of WGPA/H.

excellent angular insensitivity (Fig. 6a). For the RPA/H9.6 and BPA/H9.6 samples, although their EAB is also improved to a certain extent under oblique EMWs incidence compared with the pristine RPA and BPA samples (Fig. S27b and c), the EAB still cannot be stabilized over a wide angular range (Fig. 6b), which is attributed to the intrinsic limitations of their native aerogel pore structures. In addition, the WGPA/H3.2, WGPA/H4.8, and WGPA/H9.6 samples with different honeycomb cell sizes all exhibit outstanding angular insensitivity, with their EAB barely affected by EMWs at oblique IAs from 5° to 60° (Fig. 6c). Based on the above experimental results and systematic analysis, the superior wide-oblique-angle EMWA performance of the WGPA/H series is attributed to the synergistic effect between the radial pore structure of the waxberry-like aerogel and the boundary effect of the honeycomb arrays.

Fig. 6d elucidates the underlying EMW dissipation and absorption mechanisms, as well as the intrinsic performance advantages of WGPA/H, at the nanoscale and mesoscale, respectively.

At the nanoscale, the EMWA mechanisms of the two one-dimensional (1D) nanofillers, namely c-MWCNTs and ANFs, mainly involve the following: (I) Interfacial polarization loss: c-MWCNTs and ANFs entangle with each other via hydrogen bonding interactions, forming abundant intimately contacted heterogeneous interfaces [44]. Under a high-frequency alternating electromagnetic field, these interfaces

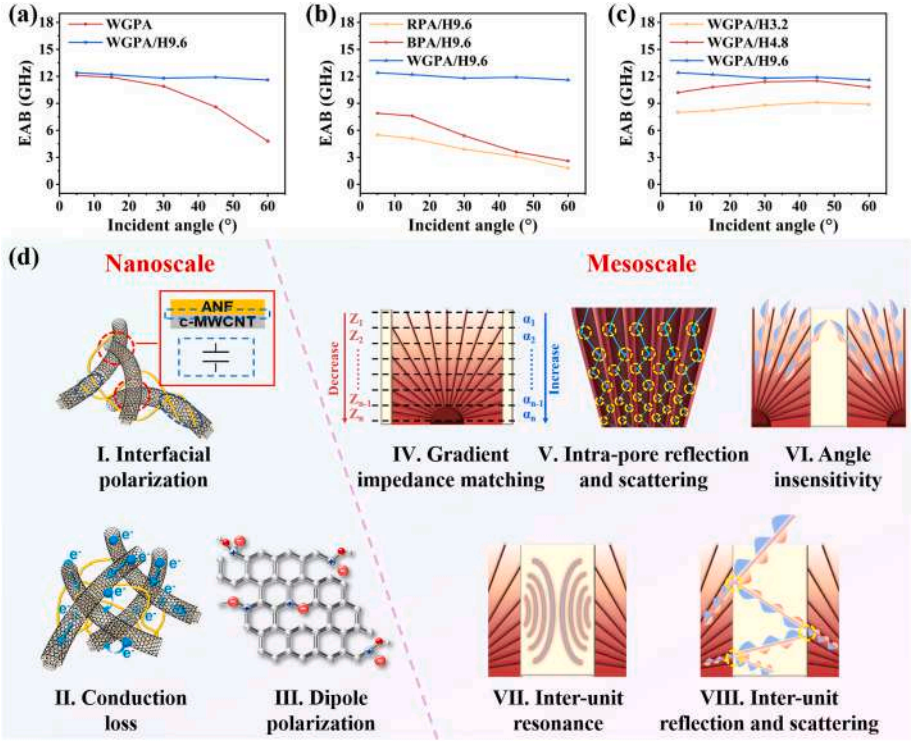

Fig. 6. Effects of (a) honeycomb skeleton, (b) aerogel pore structure, and (c) honeycomb cell size on EAB-IA. (d) EMWA mechanism analysis of WGPA/H at nanoscale and mesoscale.

trigger the oriented accumulation of space charges and dipole moment relaxation, forming capacitor-like structures that dissipate EMW energy directly into heat [45]. (II) Conductive loss: Under an alternating electromagnetic field, carriers within c-MWCNTs undergo oriented migration, high-frequency oscillation, and quantum tunneling [46]. Joule heat is generated through carrier scattering and collision, which irreversibly converts EMW energy into thermal energy for dissipation [38]. (III) Dipolar polarization loss: Carboxylation-modified c-MWCNTs are grafted with abundant polar oxygen-containing functional groups on their tube walls and open ends, and the etching effect of carboxylation introduces numerous intrinsic structural defects on the c-MWCNT tube walls. Under a high-frequency alternating electromagnetic field, the dipole active centers constructed by the polar functional groups and structural defects of c-MWCNTs undergo high-frequency rotation and relaxation with the electric field, which overcomes internal friction and energy barriers during reorientation, thus irreversibly converting the electromagnetic energy of incident EMWs into heat for dissipation [47].

At the mesoscale, the EMWA mechanisms and advantages of WGPA/H enabled by its unique hierarchical physical structure mainly include: (IV) Gradient impedance matching: The aerogel inside WGPA/H possesses a waxberry-like radial pore structure with a dense core, and the porosity of the aerogel decreases gradually from top to bottom, thus establishing a continuous gradient impedance along the z-axis [18]. The upper surface of WGPA/H exhibits high porosity with an impedance close to that of free space, which endows WGPA/H with excellent impedance-matching characteristics. This allows incident EMWs to penetrate deep into the interior of WGPA/H as much as possible, reducing EMW reflection at the free space-WGPA/H interface. As incident EMWs propagate deeper into WGPA/H along the z-axis, the porosity of the aerogel decreases further, the filler network constructed by c-MWCNTs and ANFs becomes denser, thus the corresponding impedance decreases, and its EMW dissipation capacity is significantly enhanced. (V) Multiple reflections and scattering within pores: Once incident EMWs enter the interior of WGPA/H, the trumpet-shaped pore structure of WGPA/H induces multiple reflections and scattering of EMWs at the pore wall interfaces [48]. This effect significantly prolongs the propagation path of EMWs, increases the number of interactions between EMWs and the lossy medium, and thus enhances the utilization efficiency of the material's intrinsic dielectric loss [49]. (VI) Angular insensitivity: When EMWs are obliquely incident on WGPA/H, the radial pore structure of WGPA/H enables EMWs to penetrate smoothly into the aerogel along the oblique pore channels for efficient dissipation and absorption [50]. (VII) Interunit coupling effect of honeycomb framework: Filling the aramid honeycomb with the waxberry-structured aerogel constructs periodic subwavelength resonant units. Under alternating electromagnetic fields, the interunit electric coupling effect can effectively broaden the EAB of the aerogel [51]. (VII) Multiple reflections and scattering between honeycomb units: The pristine aramid honeycomb exhibits negligible intrinsic EMWA capability, whereas WGPA/H fully exploits the synergy between the intrinsic dissipation capacity of the waxberry-structured aerogel and the multiple reflections and scattering effects between honeycomb units, thereby achieving efficient EMW dissipation and absorption [1].

3.5. Heat transfer performance and thermal stability

During the low-altitude supersonic flight of aircraft, intense frictional heat is generated between the aircraft skin and the atmosphere. To prevent thermal failure of both the skin and onboard electronic components, the thermal insulation capability and thermostability of the protective layer are critical to the service safety of aircraft.

All samples were fabricated to a uniform thickness of 10 mm. The thermal conductivities of the as-prepared aerogels and aerogel/honeycomb composites were characterized via the Hot Disk technique. To visually compare the heat transfer behavior of these materials, the bottom surface of each specimen was brought into full contact with a hot stage preheated to 100 °C. An infrared thermal camera was employed to capture the temperature evolution on the sample top surface (Fig. S28), and the average top-surface temperature was plotted as a function of heating duration.

As presented in Fig. 7a, pristine WGPA without honeycomb incorporation achieves a thermal conductivity of 59.4 mW m^{-1} K^{-1}, benefiting from its intrinsically high porosity. After embedding the honeycomb skeleton into the WGPA matrix, the thermal conductivity of WGPA/H9.6 rises to 71.6 mW m^{-1} K^{-1}. As revealed in Fig. 7c, Fig. S29a, and Fig. S29f, after 300 s of heating treatment, the top-surface temperature of pristine WGPA reaches 41.9 °C, whereas that of WGPA/H9.6 reaches 47.7 °C. This indicates a slight degradation in thermal insulation performance upon honeycomb introduction, which aligns well with the trend of the measured thermal conductivity. Moreover, the infrared thermal images show that the temperature at the honeycomb skeleton is notably higher than that of the aerogel infilled within the honeycomb pores (Figs. S29b–f), further verifying that heat propagates faster through the honeycomb skeleton than through the aerogel matrix.

For composite samples with identical honeycomb cell sizes but distinct pore architectures, the thermal conductivities of RPA/H9.6, BPA/H9.6, and WGPA/H9.6 are determined to be 63.4, 74.3, and 71.6 mW m^{-1} K^{-1}, respectively. Among the three specimens, BPA/H9.6 exhibits the highest thermal conductivity, RPA/H9.6 the lowest, and WGPA/H9.6 an intermediate value. As observed from Fig. 7d and Figs. S29b, c, f, the heating rates of BPA/H9.6 and WGPA/H9.6 are significantly higher than that of RPA/H9.6. This behavior is attributed to the oriented alignment of pore walls in BPA/H9.6 and WGPA/H9.6, which shortens the heat transfer path along the c-MWCNT thermally conductive network relative to the randomly oriented RPA/H9.6 (Figs. S30b, c, and f).

For the WGPA/H series with consistent pore structure but varying honeycomb cell sizes, the thermal conductivities of WGPA/H3.2, WGPA/H4.8, and WGPA/H9.6 are 66.4, 69.7, and 71.6 mW m^{-1} K^{-1}, respectively. As shown in Fig. 7e and Figs. S29d–f, the heating rate of WGPA/H increases progressively with increasing honeycomb cell size. Collectively, these results demonstrate a pronounced upward trend in the thermal conductivity of WGPA/H as the honeycomb cell size enlarges. For WGPA/H3.2, WGPA/H4.8, and WGPA/H9.6 samples of equal volume, the total number of waxberry-structured units remains identical, and the sole difference lies in the quantity of honeycomb cell walls. Specifically, WGPA/H3.2 contains the largest number of honeycomb cell walls within a single waxberry-structured unit. As heat propagates along the radial pore walls of WGPA/H3.2, it undergoes the most frequent obstruction from honeycomb cell walls and the greatest number of thermal scattering events, resulting in the lowest heat transfer efficiency (Fig. S30d). Conversely, the waxberry-structured units in WGPA/H9.6 are well size-matched to the honeycomb cells, such that heat transfer along their radial pore walls is barely hindered by the honeycomb walls (Fig. S30f). Consequently, WGPA/H9.6 demonstrates the highest heat transfer efficiency among the series.

Furthermore, numerical simulations of the thermal conduction behavior of aerogel/honeycomb composites were performed via COMSOL Multiphysics under an identical heat source and fixed heating duration (Fig. S31). The detailed modeling and simulation parameters

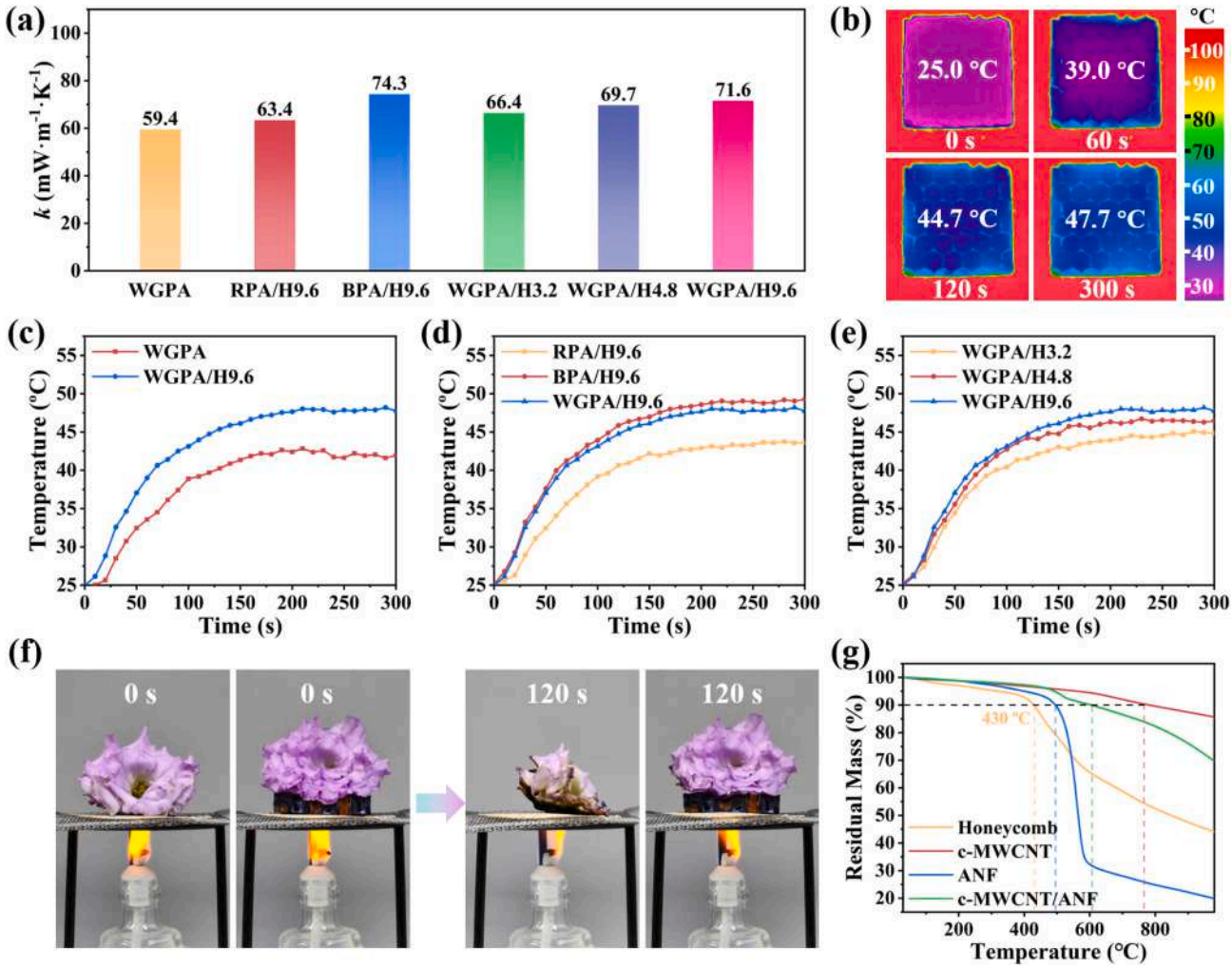

Fig. 7. (a) Thermal conductivities of the samples. (b) Infrared thermal images of WGPA/H9.6 on a hot stage at 100 °C. (c–e) Temperature-time curves of the upper surfaces of the samples. (f) Demonstration of thermostability and thermal insulation performance of WGPA/H. (g) TGA curves of constituent materials.

are provided in the Supporting Information. Figs. S31b, c, e, f, i, and l present the temperature distribution profiles and isotherm plots of the composite models with a fixed honeycomb cell size but varied pore architectures (RPA/H9.6, BPA/H9.6, and WGPA/H9.6). It can be observed that RPA/H9.6 exhibits the lowest heat transfer rate. In addition, the heat transfer rate within the honeycomb framework is higher than that inside the aerogel matrix, which is consistent with the infrared thermal imaging results. To further elucidate the effect of honeycomb cell size on thermal transport, Figs. S31g–l displays the temperature distribution profiles and isotherm plots of the composite models with different honeycomb cell sizes (WGPA/H3.2, WGPA/H4.8, and WGPA/H9.6). It is evident that heat conduction along the radial pore channels is impeded by the honeycomb walls.

Moreover, WGPA/H exhibits excellent thermostability. As shown in Fig. 7f, when fresh flowers were placed directly on an asbestos wire gauze heated by an alcohol lamp, the flowers rapidly wilted and carbonized under the intense heating of the flame. In contrast, when a 10 mm-thick WGPA/H was positioned beneath the fresh flowers as a thermal barrier, the flowers could maintain their original morphology for an extended period. In addition, the thermal degradation temperatures of the constituent materials were accurately determined using thermogravimetric analysis (TGA) under a flowing nitrogen atmosphere. Herein, the thermal degradation temperature (TDT) is defined as the temperature corresponding to 90% residual mass relative to the initial mass. As shown in Fig. 7g, the TDTs of the honeycomb, c-MWCNT, ANF, and c-MWCNT/ANF composite were 430 °C, 782 °C, 495 °C, and 604 °C, respectively. This excellent thermal degradation resistance endows WGPA/H with favorable application prospects for service in extremely high-temperature environments.

3.6. Mechanical property

High mechanical strength is a critical prerequisite to ensure the service safety of aircraft. In this work, the compressive strength of the pristine aerogels, honeycombs, and aerogel/honeycomb composites along the z-axis was characterized using a universal testing machine within a strain range of 0–15%. As shown in Fig. 8a, the compressive strength of the honeycomb-free WGPA sample increased gradually with increasing strain, reaching 30.6 kPa at a strain of 15%. In contrast, following the incorporation of the honeycomb skeleton into the aerogel

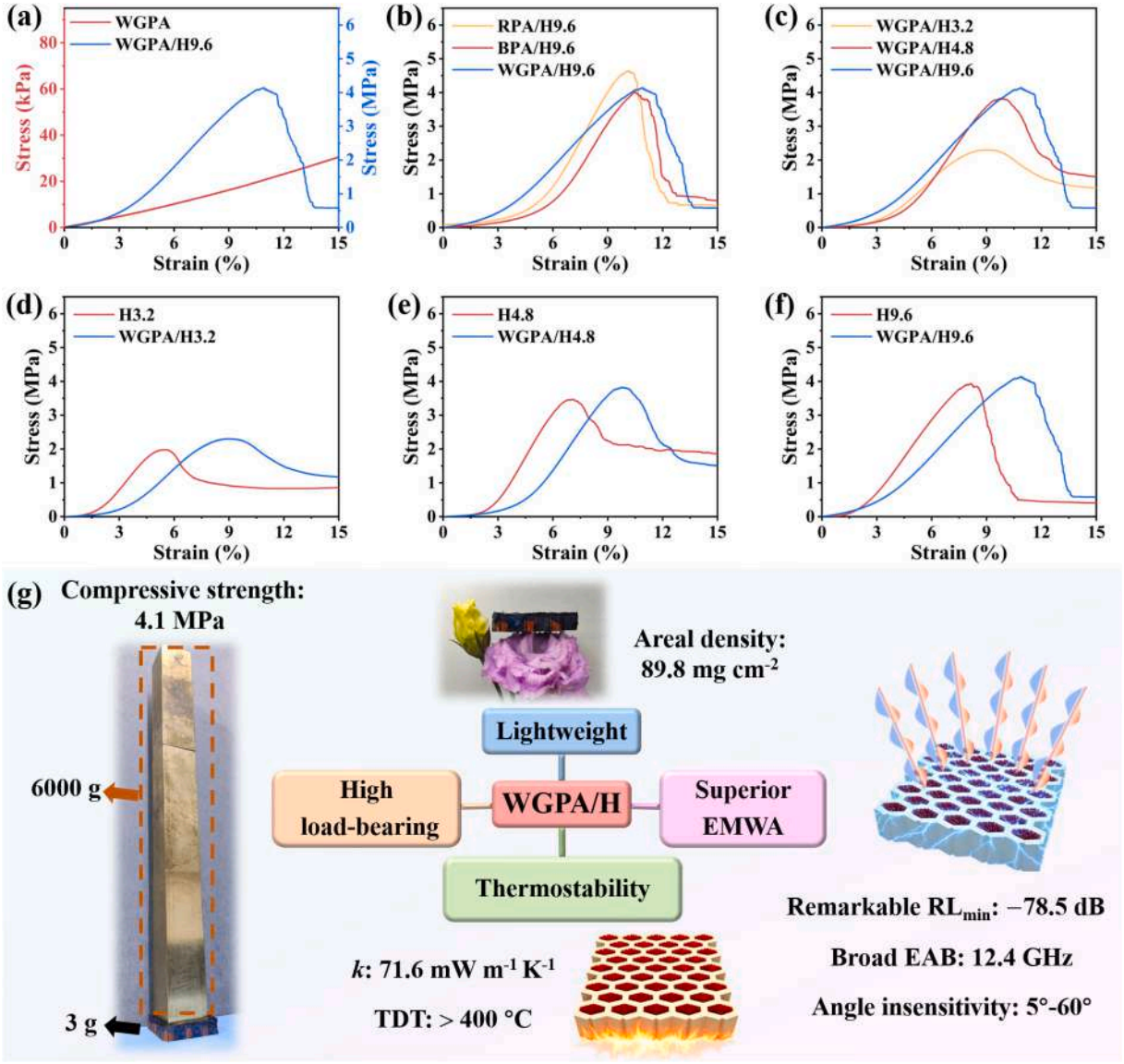

Fig. 8. Compressive stress-strain curves. (a) With and without embedded honeycomb skeleton. (b) Aerogels with different pore structures. (c) Honeycombs with different cell sizes. (d–f) Comparison of pristine honeycombs with WGPA/H metamaterials. (g) Multifunctionality of WGPA/H.

matrix, the maximum compressive strength of the WGPA/H9.6 sample increased to 4.1 MPa, which is two orders of magnitude higher than that of the pristine WGPA sample. This result demonstrates that the incorporation of the honeycomb skeleton drastically enhances the compression resistance of the samples, enabling the inherently brittle aerogel to be applied in high-load service scenarios. Fig. 8b presents the compressive stress-strain curves of composite samples with an identical honeycomb cell size but distinct aerogel pore structures. The maximum compressive strengths of the RPA/H9.6, BPA/H9.6, and WGPA/H9.6 samples were 4.6 MPa, 4.0 MPa, and 4.1 MPa, respectively. Fig. S32 and Fig. 8c illustrate the maximum compressive strengths of the pristine honeycombs with different cell sizes and the corresponding WGPA/H metamaterials. Specifically, the maximum compressive strengths of the pristine H3.2, H4.8, and H9.6 honeycomb samples were 2.0 MPa, 3.5 MPa, and 3.9 MPa, respectively, while those of the WGPA/H3.2, WGPA/H4.8, and WGPA/H9.6 samples were 2.3 MPa, 3.8 MPa, and 4.1 MPa, respectively. These results reveal that the maximum compressive strength of the samples exhibits a monotonically increasing trend with the enlargement of honeycomb cell size. In addition, further analysis of Figs. 8d–f reveals that the maximum compressive strength of WGPA/H is consistently superior to that of the pristine honeycombs with the same cell size. This finding indicates that the infilled aerogel can also enhance the compression resistance of the honeycomb skeleton to a certain extent. WGPA/H is capable of bearing a load up to 2000 times its own weight (Fig. 8g).

To extend the cruising range of aircraft, minimizing airframe weight is critically imperative, and thus the lightweight design of EMWA protective layers is of remarkable scientific significance and engineering value. The as-prepared WGPA/H exhibits an ultralow areal density of merely 89.8 mg cm^{-2}. As illustrated in Fig. 8g, it rests stably on flower petals without causing any deformation, which unambiguously validates its exceptional ultra-lightweight characteristic.

Regarding the synergistic and trade-off relationships among EMWA, thermal management, and mechanical load-bearing performance: WGPA/H achieves synergistic enhancement between EMWA and mechanical performance through the coupling of the gradient pore structure and the periodic honeycomb skeleton. Compared with the pristine WGPA aerogel, the compressive strength of WGPA/H9.6 increased from 30.6 kPa to 4.1 MPa, corresponding to an approximately 130-fold enhancement. Meanwhile, RL_{min} was significantly optimized from −40.9 dB to −78.5 dB, and EAB was slightly broadened from 12.1 GHz to 12.4 GHz. The improvement in mechanical performance arises from the rigid honeycomb skeleton that bears the main load and provides reliable protection for the internal aerogel. The enhancement in EMWA performance is attributed to the inter-unit coupling resonance of the periodic honeycomb array and the additional multiple scattering effects at the honeycomb wall–aerogel interfaces. While enhancing the mechanical strength and electromagnetic performance, the honeycomb skeleton forms preferential heat conduction pathways, resulting in a slight decrease in the thermal insulation performance of WGPA/H9.6 compared with the pristine WGPA aerogel. Nevertheless, WGPA/H9.6 can still satisfy the thermal protection requirements of the vast majority of aerospace scenarios. At the cost of a minor loss in thermal insulation performance, WGPA/H9.6 gains improvements in both mechanical strength and EMWA performance, which represents a highly cost-effective trade-off in practical engineering applications.

4. Conclusion

In summary, we innovatively proposed an integrated fabrication strategy combining the dot-matrix cold-source ice-templating method with a honeycomb skeleton, and controllably fabricated the WGPA/H metamaterial. Through systematic experimental characterizations and finite element simulations, we revealed the underlying regulation mechanism of core parameters (including the presence/absence of honeycomb skeleton, aerogel hierarchical pore structure, and honeycomb cell size) on the EMWA, heat transfer, and mechanical properties of the as-prepared aerogel/honeycomb composite devices. The results demonstrated that WGPA/H successfully breaks the long-standing trade-off between interfacial impedance matching and internal electromagnetic dissipation in EMWA devices, via the synergistic coupling effect between the gradient impedance constructed by the waxberry-like hierarchical pore structure and the honeycomb array. WGPA/H delivered an exceptional RL_{min} of −78.5 dB and an ultrabroad EAB of 12.4 GHz, along with excellent EMWA stability to obliquely incident EMWs over a wide IA range of 5° to 60°. Furthermore, WGPA/H exhibited superior thermostability, enabling it to withstand the extreme and complex service environments. Most notably, WGPA/H features an ultralow areal density of only 89.8 mg·cm^{-2}, while delivering a high compressive strength up to 4.1 MPa, benefiting from the reinforcing effect of the honeycomb skeleton. This comprehensive performance well matches the core application requirements of lightweight, high load-bearing, and multifunctional integration for aircraft, endowing WGPA/H with broad engineering application prospects and commercialization value in aerospace electromagnetic protection and stealth fields.

CRediT authorship contribution statement

Anping Wang: Writing – review & editing, Writing – original draft, Visualization, Methodology, Investigation, Formal analysis, Data curation, Conceptualization. **Zhichun Zhang:** Writing – review & editing, Validation, Resources, Project administration. **Zibo Li:** Writing – review & editing. **Yanju Liu:** Writing – review & editing, Supervision, Resources, Project administration, Funding acquisition. **Jinsong Leng:** Writing – review & editing, Supervision, Resources, Project administration.

Declaration of competing interest

The authors declare that they have no known competing financial interests or personal relationships that could have appeared to influence the work reported in this paper.

Acknowledgements

This work was financially supported by the National Natural Science Foundation of China (Granted No. 92271206).

Appendix A. Supplementary data

Supplementary data to this article can be found online at https://doi.org/10.1016/j.cej.2026.180386.

Data availability

Data will be made available on request.

References

[1] G. Wang, D. Li, W. Liao, T. Liu, *Agile stealth: bioinspired metamaterials with continuous dynamic tuning*, Adv. Mater. 38 (2) (2026) e11070, https://doi.org/10.1002/adma.202511070.

[2] X. Zhou, S. Li, H. Xi, P. Zhong, J. Sun, Z. Wang, J. Liu, H. Wu, Construction of 0D/2D heterojunction in 3D MXene/GQDs hybrid aerogels for enhanced broad electromagnetic wave absorption, J. Alloys Compd. 1016 (2025) 179021, https://doi.org/10.1016/j.jallcom.2025.179021.

[3] G. Qin, Y. Liu, Y. Yan, Z. Cheng, G. Ma, K. Zhang, X. Huang, Combined experiment and simulation on pore structure of graphene aerogel for microwave absorption and thermal insulation, Compos. Part B Eng. 298 (2025) 112397, https://doi.org/10.1016/j.compositesb.2025.112397.

[4] X. Zhang, Z. Wang, G. Zhou, J. Li, C. Li, C. Lin, X. Xin, Multifunctional metamaterials based on MXene composite aerogels for integrated load-bearing and multiphysics wave attenuation, Compos. Part B Eng. 309 (2026) 113075, https://doi.org/10.1016/j.compositesb.2025.113075.

[5] S. Huang, Y. Liu, K. Wen, X. Su, C. Liang, H. Duan, G. Zhao, Optimization design of a novel microwave absorbing honeycomb sandwich structure filled with magnetic shear-stiffening gel, Compos. Sci. Technol. 232 (2023) 109883, https://doi.org/10.1016/j.compscitech.2022.109883.

[6] B. Jiang, J. Shang, N. Li, Y. Wang, Z. Hu, J. Yu, Aramid honeycomb composites filled with rGO/BC aerogel for broadband microwave absorption and multifunctional applications, Compos. Commun. 58 (2025) 102512, https://doi.org/10.1016/j.coco.2025.102512.

[7] X. Su, X. Gao, J. Wang, Y. Zhang, Y. Liu, Y. Liu, Multifunctional broadband electromagnetic wave absorption through structural engineering of hierarchical aerogel-honeycomb metacomposites, Carbon 243 (2025) 120517, https://doi.org/10.1016/j.carbon.2025.120517.

[8] M. Yu, X. Chen, J. Liu, P. Wu, D. Li, J. Lu, A. Xie, C. Yu, Gradient magneto-dielectric heterostructured aerogels with MXene hollow spheres for integrated electromagnetic-thermal management, J. Colloid Interface Sci. 712 (2026) 140119, https://doi.org/10.1016/j.jcis.2026.140119.

[9] S. Wang, Z. Cheng, Y. Yan, J. Yao, Y. Liu, J. Tao, L. Duan, Y. Weng, H. Zhu, H. Zhuang, J. Zhou, X. Hao, Programmable electromagnetic switching in shape-memory-driven liquid metal/polyimide/aramid nanofiber aerogels for intelligent wave management, Adv. Funct. Mater. 36 (22) (2026) e21612, https://doi.org/10.1002/adfm.202521612.

[10] A. Wang, Z. Zhang, Y. Liu, J. Leng, Waxberry-inspired aerogel metamaterial with gradient pore structure for superior electromagnetic wave absorption, Compos. Part B Eng. 313 (2026) 113399, https://doi.org/10.1016/j.compositesb.2026.113399.

[11] Y. Gao, Z. Lei, L. Pan, Q. Wu, X. Zhuang, G. Tan, M. Ning, Q. Man, Lightweight chitosan-derived carbon/rGO aerogels loaded with hollow $Co_{1-x}Ni_xO$ nanocubes for superior electromagnetic wave absorption and heat insulation, Chem. Eng. J. 457 (2023) 141325, https://doi.org/10.1016/j.cej.2023.141325.

[12] C. Gao, D. Gou, G. Huang, Z. Zhang, J. Wei, F. Gao, Y. Zhang, M. Terrones, X. Chen, Y. Wang, Spiderweb-structured aerogels with high-efficiency microwave absorption and multifunctionality, Nano Energy 138 (2025) 110863, https://doi.org/10.1016/j.nanoen.2025.110863.

[13] F. Yin, H. Lin, W. Wang, L. Zhao, R. Paul, J. Li, W. Liu, D. Kong, Y. Jiang, C. Hu, Multifunctional anisotropic aerogels for intelligent electromagnetic wave absorption, Adv. Funct. Mater. 35 (14) (2025) 2418257, https://doi.org/10.1002/adfm.202418257.

[14] Y. Mao, Y. Sheng, H. Sun, C. Yang, J. Liu, Y. Wang, K. Zhang, C. Tang, S. Fu, Multiscale structural engineering of cellulose-derived carbon aerogel metamaterials for broadband microwave absorption, Small 22 (10) (2026) e12149, https://doi.org/10.1002/smll.202512149.

[15] W. Gu, Z. Luo, J. Wang, X. Tan, Z. Tao, P. Zhou, H. Zhang, D. Lan, A. Xia, Multifunctional lightweight rGO/polyimide hybrid aerogels for highly efficient infrared-radar-acoustic compatibility via heterogeneous interface engineering strategies, J. Mater. Sci. Technol. 243 (2026) 102–114, https://doi.org/10.1016/j.jmst.2025.04.024.

[16] B.-X. Wang, C. Xu, G. Duan, W. Xu, F. Pi, Review of broadband metamaterial absorbers: from principles, design strategies, and tunable properties to functional applications, Adv. Funct. Mater. 33 (14) (2023) 2213818, https://doi.org/10.1002/adfm.202213818.

[17] J. Lin, L. Wang, W. Chu, H. Yu, Z. Chen, M. Chen, W. Song, X. Gu, J. Liu, N. Wu, Z. Zeng, Ultrabroadband low-frequency microwave absorption in multiscale aerogel-metamaterial hybrids, Adv. Funct. Mater. 36 (36) (2026) e27401, https://doi.org/10.1002/adfm.202527401.

[18] N. Qu, H. Sun, Y. Sun, M. He, R. Xing, J. Gu, J. Kong, 2D/2D coupled MOF/Fe composite metamaterials enable robust ultra–broadband microwave absorption, Nat. Commun. 15 (1) (2024) 5642, https://doi.org/10.1038/s41467-024-49762-4.

[19] W. Ma, X. Liu, T. Yang, J. Wang, Z. Qiu, Z. Cai, P. Bai, X. Ji, Y. Huang, Strong magnetic–dielectric synergistic gradient metamaterials for boosting superior multispectral ultra-broadband absorption with low-frequency compatibility, Adv. Funct. Mater. 35 (18) (2025) 2314046, https://doi.org/10.1002/adfm.202314046.

[20] Y. Wu, C. An, Y. Guo, Y. Zong, N. Jiang, Q. Zheng, Z.-Z. Yu, Highly aligned graphene aerogels for multifunctional composites, Nano Micro Lett. 16 (1) (2024) 118, https://doi.org/10.1007/s40820-024-01357-w.

[21] J. Wei, G. Shao, X. Huang, Freeze-cast Ni-MOF nanobelts/chitosan-derived magnetic carbon aerogels for broadband electromagnetic wave absorption, ACS Appl. Mater. Interfaces 16 (16) (2024) 20969–20979, https://doi.org/10.1021/acsami.4c03543.

[22] X. Wang, X. Chen, Q. He, Y. Hui, C. Xu, B. Wang, F. Shan, J. Zhang, J. Shao, Bidirectional, multilayer MXene/polyimide aerogels for ultra-broadband microwave absorption, Adv. Mater. 36 (36) (2024) 2401733, https://doi.org/10.1002/adma.202401733.

[23] C. Liu, Z. Zeng, J. Qiao, Q. Wu, W. Liu, F. Gao, J. Liu, Versatile cellulose nanofibril assisted preparation of ultralight, scalable carbon nanotube aerogel-based electromagnetic wave absorbers with ultrahigh reflection loss, Carbon 213 (2023) 118277, https://doi.org/10.1016/j.carbon.2023.118277.

[24] H. Wu, X. Ren, W. Hu, Y. Tang, H. Yin, H. Fan, H. Yuan, C. Wang, Y. Xin, Permittivity controllable CNTs/PI composite aerogels with oriented microchannels for advanced microwave absorption and thermal isolation, Carbon 233 (2025) 119883, https://doi.org/10.1016/j.carbon.2024.119883.

[25] W. Cao, L. Yang, X. Qi, Y. Hou, J. Zhu, M. Yang, Carbon nanotube wires sheathed by aramid nanofibers, Adv. Funct. Mater. 27 (34) (2017) 1701061, https://doi.org/10.1002/adfm.201701061.

[26] H. Wei, T. Lei, W. Li, Lightweight, flexible, heat resistant and thermal insulating aramid nanofiber/magnetic carbon nanotube interpenetrating network aerogel for microwave absorption in complex environments, Carbon 225 (2024) 119115, https://doi.org/10.1016/j.carbon.2024.119115.

[27] A. Wang, X. Zhang, F. Chen, Q. Fu, Aramid nanofiber framework supporting graphene nanoplate via wet-spinning for a high-performance filament, Carbon 179 (2021) 655–665, https://doi.org/10.1016/j.carbon.2021.04.056.

[28] M. Wang, S. Hu, S. Bae, V. Cecen, A.E. Emre, Z. Zhong, L. Liu, C. Heltzel, Y. Huang, N.A. Kotov, Aramid nanofiber aerogels: versatile high complexity components for multifunctional composites, Adv. Mater. 37 (38) (2025) 2502508, https://doi.org/10.1002/adma.202502508.

[29] J. Zhou, W. Liu, L. Lv, X. Lu, M. Liu, L. Jiang, Dual deprotonation-enabled 3D hydrogen-bonding networks in aramid nanofiber films toward extraordinary mechanical strength and ultralow thermal conductivity, Adv. Funct. Mater. 36 (1) (2026) e09681, https://doi.org/10.1002/adfm.202509681.

[30] B. Zhang, Z. Qu, C. Ruiz-Agudo, L. Yang, B. Chi, Y. Kong, F. Wang, Lightweight magnetic carbon nanotube/cellulose nanofibre aerogels with microstructure engineering for enhanced microwave absorption, Carbon 234 (2025) 120020, https://doi.org/10.1016/j.carbon.2025.120020.

[31] Z. Luo, P. Han, B. Yu, W. Yan, X. Chen, Y. Feng, H. Zheng, H. Guo, Z. Cheng, J. He, RGO/ANFs composite fibers with dual functions of thermal conductivity and electromagnetic shielding of lotus root structure based on sol-gel wet spinning, Carbon 226 (2024) 119142, https://doi.org/10.1016/j.carbon.2024.119142.

[32] J. Huang, J. Li, X. Xu, L. Hua, Z. Lu, In situ loading of polypyrrole onto aramid nanofiber and carbon nanotube aerogel fibers as physiology and motion sensors, ACS Nano 16 (5) (2022) 8161–8171, https://doi.org/10.1021/acsnano.2c01540.

[33] L. Yin, B. Zhang, M. Tian, N. Ning, L. Zhang, W. Wang, Surface construction of ANF/CNT onto aramid fibers to enhance interfacial adhesion and provide real-time monitoring of deformation, Compos. Sci. Technol. 223 (2022) 109336, https://doi.org/10.1016/j.compscitech.2022.109336.

[34] J. Zhu, W. Cao, M. Yue, Y. Hou, J. Han, M. Yang, Strong and stiff aramid nanofiber/carbon nanotube nanocomposites, ACS Nano 9 (3) (2015) 2489–2501, https://doi.org/10.1021/nn504927e.

[35] F. Jia, Z. Lu, Y. Liu, J. Li, F. Xie, J. Dong, Carboxylate-decorated multiwalled carbon nanotube/aramid nanofiber film for tunable electromagnetic interference shielding performance and rapid electric heating capacity, ACS Appl. Polym. Mater. 4 (9) (2022) 6342–6353, https://doi.org/10.1021/acsapm.2c00570.

[36] Y. Zou, Z. Chen, X. Guo, Z. Peng, C. Yu, W. Zhong, Mechanically robust and elastic graphene/aramid nanofiber/polyaniline nanotube aerogels for pressure sensors, ACS Appl. Mater. Interfaces 14 (15) (2022) 17858–17868, https://doi.org/10.1021/acsami.2c02538.

[37] D. Zhang, W. Song, L. Lv, C. Gao, F. Gao, H. Guo, R. Diao, W. Dai, J. Niu, X. Chen, J. Wei, M. Terrones, Y. Wang, Mono-dispersion decorated ultra-long single-walled carbon nanotube/aramid nanofiber for high-strength electromagnetic interference shielding film with Joule heating properties, Carbon 214 (2023) 118315, https://doi.org/10.1016/j.carbon.2023.118315.

[38] H. Yu, J. Yao, J. Lv, R. Zhang, Z. Wang, X. Song, X. Wei, J. Zhou, Low-temperature carbonization MOF/CNF aerogel for high-performance microwave absorption and thermal camouflage, Carbon 243 (2025) 120485, https://doi.org/10.1016/j.carbon.2025.120485.

[39] J. Cheng, L. Cai, Y. Shi, F. Pan, Y. Dong, X. Zhu, H. Jiang, X. Zhang, Z. Xiang, W. Lu, Polarization loss-enhanced honeycomb-like MoS_2 nanoflowers/*Undaria pinnatifida*-derived porous carbon composites with high-efficient electromagnetic wave absorption, Chem. Eng. J. 431 (2022) 134284, https://doi.org/10.1016/j.cej.2021.134284.

[40] Z. Tian, F. Hu, P. Zhang, Y. Fan, A.S. Shamshirgar, S. Wu, L. Cai, Y. Bai, X. Wu, J. Rosen, Z. Sun, High-entropy engineering of A-site in MAX phases toward superior microwave absorption properties, Matter 8 (12) (2025) 102367, https://doi.org/10.1016/j.matt.2025.102367.

[41] H. Lv, Z. Yang, H. Pan, R. Wu, Electromagnetic absorption materials: current progress and new frontiers, Prog. Mater. Sci. 127 (2022) 100946, https://doi.org/10.1016/j.pmatsci.2022.100946.

[42] Z. Guo, F. Wang, Z. Zong, T. Wu, S. Liu, F. Ren, D. Yan, P. Ren, H. Wu, Hierarchically dielectric-magnetic hybrid aerogels with plentiful heterointerfaces for high-efficiency electromagnetic wave absorption and thermal insulation, Chem. Eng. J. 525 (2025) 170586, https://doi.org/10.1016/j.cej.2025.170586.

[43] X. Yin, Y. Wang, N. Pang, C. Liu, Y. Xu, M. Yu, C. Zhou, Ultralight, highly elastic ZrO_2/carbon fiber reinforced reduced graphene oxide aerogels with radar and infrared stealth capabilities, Compos. Part B Eng. 303 (2025) 112628, https://doi.org/10.1016/j.compositesb.2025.112628.

[44] A. Wang, Z. Zhang, Y. Liu, Z. Li, J. Leng, Lightweight carbon nanotube/aramid nanofiber aerogel with superior electromagnetic wave absorption, thermal insulation, and flame resistance, Carbon 225 (2024) 119105, https://doi.org/10.1016/j.carbon.2024.119105.

[45] J. Tang, F. Guo, M. Ni, X. Guan, C. Liu, G. Ji, 3D-engineered MXene aerogels for lightweight microwave absorption and infrared stealth, J. Alloys Compd. 1046 (2025) 184891, https://doi.org/10.1016/j.jallcom.2025.184891.

[46] X. Wu, Y. Deng, X. Zhang, N. Xu, T. Liu, P. Zhang, T. You, S. Zhang, C. Han, B. Wang, Y. Wang, High-temperature-stable CNT/SiC ultrafine fibers with superior electromagnetic-wave-absorbing performance via CNT-driven multiple lossy phase modulation, Chem. Eng. J. 537 (2026) 176406, https://doi.org/10.1016/j.cej.2026.176406.

[47] Y. Zhang, H. Si, Z. Dai, W. Zhang, B. Hao, C. Li, J. Zhang, C. Gong, Subwavelength-scale graphene aerogel powders for efficient microwave absorption composites with improved mechanical strength, Chem. Eng. J. 505 (2025) 159118, https://doi.org/10.1016/j.cej.2024.159118.

[48] C. Zhang, W. Yang, Z. Li, K. Yang, L. Kong, S. Du, J. Dong, W. Zhu, R. Feng, Z. Ma, Y. Li, Enhancing low-frequency electromagnetic wave absorption via induced

polarization in honeycomb-structured graphene/polymer flexible fibers, Chem. Eng. J. 535 (2026) 175183, https://doi.org/10.1016/j.cej.2026.175183.
[49] Y. Zhao, N. Ahmad, Y. Yang, W. Zhai, Mechanical-dielectric optimized graphene aerogels with strain-tunable microwave attenuation and shielding functions, J. Mater. Chem. A (2024), https://doi.org/10.1039/D4TA06820C.
[50] X. Sun, M. Yang, S. Yang, S. Wang, W. Yin, R. Che, Y. Li, Ultrabroad band microwave absorption of carbonized waxberry with hierarchical structure, Small 15 (43) (2019) 1902974, https://doi.org/10.1002/smll.201902974.
[51] X. Sun, Y. Li, Y. Huang, Y. Cheng, S. Wang, W. Yin, Achieving super broadband electromagnetic absorption by optimizing impedance match of rGO sponge metamaterials, Adv. Funct. Mater. 32 (5) (2022) 2107508, https://doi.org/10.1002/adfm.202107508.